

THESIS FOR THE DEGREE OF DOCTOR OF PHILOSOPHY

Alloy Design for High-Entropy Alloys: Predicting Solid Solubility, and  
Balancing Mechanical Properties and Oxidation Resistance

SAAD SHEIKH



Department of Industrial and Materials Science  
CHALMERS UNIVERSITY OF TECHNOLOGY  
Gothenburg, Sweden 2018

Alloy Design for High-Entropy Alloys: Predicting Solid Solubility, and  
Balancing Mechanical Properties and Oxidation Resistance  
SAAD SHEIKH

© Saad Sheikh, 2018

ISBN: 978-91-7597-762-1  
Doktorsavhandlingar vid Chalmers tekniska högskolan  
Ny serie Nr 4443  
ISSN 0346-718X

Department of Industrial and Materials Science  
Chalmers University of Technology  
SE-41296 Gothenburg  
Sweden  
Tel: +46 31 772 1000

***Cover images:***

**Left:** Cross sectional microstructure of the as-aluminized sample.

**Middle:** Cross sectional microstructure of the aluminized sample after oxidation.

**Right:** SEM-EDS elemental map of the aluminized sample after oxidation, indicating the formation of an oxide layer.

Printed by Chalmers Reproservice

Gothenburg, Sweden 2018

**Dedicated to:**

Those of you who are struggling.



# Alloy Design for High-Entropy Alloys: Predicting Solid Solubility, and Balancing Mechanical Properties and Oxidation Resistance

SAAD SHEIKH

Department of Industrial and Materials Science  
Chalmers University of Technology

## Abstract

High-entropy alloys (HEAs) comprise of multi-principal elements in equi-atomic or near equi-atomic percentage. HEAs are considered as potential structural materials for high temperature applications, which require alloy design for optimum mechanical properties. In this regard, achieving both high strength and tensile ductility is still a great challenge. Compared to conventional alloys, HEAs have high configurational entropy, which tends to stabilize the solid solution formation, mainly face-centered-cubic (fcc) and/or body-centered-cubic (bcc) solid solutions. Generally, fcc-type HEAs are ductile but soft, while bcc-type HEAs are hard but brittle.

This project has three working directions. The first part of this work is related to alloy design and aims to gain improved understanding of the solid solubility in HEAs. The difficulties that are encountered by HEAs are mostly related to the alloy design strategy. Previous approaches to describe the solid solubilities in HEAs could not accurately locate the solubility limit. Therefore, the need for single-phase solid solution and controlling the formation of secondary phases is addressed through the molecular orbital approach. The output of this approach is the introduction of the  $Md$  parameter, the d-orbital energy level to HEAs, which can well describe the solubility limit in HEAs. To further develop this approach,  $Md$  is also complemented with theoretical methods specifically, CALPHAD and experimental work.

The second part of this work is to ductilize HEAs containing group IV (Ti, Zr, Hf), V (V, Nb, Ta) and VI (Cr, Mo, W) refractory elements, known as refractory HEAs (RHEAs), where inadequate ductility puts a limit on their mechanical performance for structural applications. A strategy is proposed to design RHEAs with sufficient yield strength combined with ductility at room temperature. Ductility is introduced by maintaining the bcc single-phase solid solution and keeping the number of total valence electrons low, which can be achieved through controlled alloying. More importantly, a mechanism and route for ductilizing RHEAs is proposed.

The third part, which is the ultimate goal of this work, is to address the balance of mechanical properties and oxidation resistance for RHEAs, for the optimal development of RHEAs aiming at high-temperature applications. Based on the known facts for refractory alloys, the oxidation resistance is also problematic for RHEAs and there exists only limited work towards the study of high temperature oxidation of ductile RHEAs. Therefore, the oxidation mechanism is studied and it is found out that the insufficient oxidation resistance in existing ductile RHEAs is attributed to the failure in forming protective oxide scales accompanied by the accelerated internal oxidation leading to pest-disintegration or pesting. Efforts are also carried out to improve oxidation resistance via alloying and pack-cementation aluminizing. These studies provide important input to the further development of RHEAs as novel high-temperature materials and shed light on the design of refractory HEAs with optimal mechanical and oxidation resistance properties.

**Keywords:** High-entropy alloys; alloy design; ductility; mechanical properties; refractory high-entropy alloys; valence electron concentration; oxidation resistance; pesting; internal oxidation; aluminizing

## Preface

This doctoral thesis is performed at the Department of Industrial and Materials Science (previously Materials and Manufacturing Technology), Chalmers University of Technology during the period November 2013-May 2018. This work is funded by Area of Advance Materials, Chalmers, and is carried out under the supervision of Associate Professor Sheng Guo and with Professor Uta Klement as examiner. Part of the activities in paper IV and V were carried out at The Hong Kong Polytechnic University and National Institute for Materials Science (NIMS), Tsukuba, Japan.

## List of Appended Papers

**Paper I:** Saad Sheikh, Uta Klement, and Sheng Guo. Predicting the Solid Solubility Limit in High-Entropy Alloys Using the Molecular Orbital Approach. *J. Appl. Phys.* 118, 194902 (2015)

**Paper II:** Saad Sheikh, Huahai Mao and Sheng Guo. Predicting solid solubility in  $\text{CoCrFeNiM}_x$  ( $M = 4d$  transition metal) high-entropy alloys. *J. Appl. Phys.* 121, 194903 (2017)

**Paper III:** Saad Sheikh, Samrand Shafeie, Qiang Hu, Johan Ahlström, Christer Persson, Jaroslav Veselý, Jiří Zýka, Uta Klement, Sheng Guo. Alloy Design for Intrinsically Ductile Refractory High-Entropy Alloys. *J. Appl. Phys.* 120, 164902 (2016)

**Paper IV:** Saad Sheikh, Muhammad Kurnia Bijaksana, Amir Motallebzadeh, Samrand Shafeie, Adrianna Lozinko, Lu Gan, Te-Kang Tsao, Uta Klement, Demircan Canadinc, Hideyuki Murakami, Sheng Guo. Accelerated Oxidation in Ductile Refractory High-Entropy Alloys. *Intermetallics*, 97, 58-66 (2018)

**Paper V:** Saad Sheikh, Lu Gan, Te-Kang Tsao, Hideyuki Murakami, Samrand Shafeie, Sheng Guo. Aluminizing for Enhanced Oxidation Resistance of Ductile Refractory High-Entropy Alloys, manuscript in preparation.

# Table of Contents

<b>1 Introduction</b> .....	1
1.1 Aim for this study .....	2
1.2 Research goals .....	4
<b>2 High-entropy alloys</b> .....	7
2.1 Introduction of high-entropy alloys .....	7
2.2 Key characteristics of HEAs .....	8
<b>3 Alloy design and current challenges to HEAs</b> .....	13
3.1 The <i>Md</i> parameter .....	15
3.2 <i>Md</i> and Thermo-Calc .....	20
3.3 <i>Md</i> and mechanical properties .....	21
3.4 Mechanical properties of HEAs .....	22
3.4.1 Properties under tensile testing .....	24
3.4.2 Beyond tensile properties .....	25
3.5 Refractory high-entropy alloys (RHEAs) .....	26
3.6 Theories for ductility .....	30
3.7 Thermo-mechanically treated RHEAs .....	32
3.8 Oxidation resistance of RHEAs with optimum mechanical properties .....	33
3.9 Accelerated oxidation and alloying .....	34
3.10 Aluminizing .....	37
<b>4 Experimental methods</b> .....	43
4.1 Arc melting .....	43
4.2 Vickers hardness measurements .....	43
4.3 X-ray diffraction .....	43
4.4 Oxidation studies .....	44
4.5 Microstructural investigation .....	44
4.6 Tensile testing .....	46
4.7 Aluminizing .....	46
<b>5 Summary of Results</b> .....	49
5.1 The <i>Md</i> concept and HEAs .....	49
5.2 VEC and RHEAs .....	53

5.3 Thermomechanically treated $\text{Hf}_{0.5}\text{Nb}_{0.5}\text{Ta}_{0.5}\text{Ti}_{1.5}\text{Zr}$ .....	59
5.4 Oxidation studies for ductile RHEA .....	61
5.5 Aluminizing studies for ductile RHEA .....	65
5.5.1 Oxidation resistance for aluminized $\text{Hf}_{0.5}\text{Nb}_{0.5}\text{Ta}_{0.5}\text{Ti}_{1.5}\text{Zr}$ .....	65
5.5.2 Oxidation resistance for aluminized $\text{Al}_{0.5}\text{Cr}_{0.25}\text{Nb}_{0.5}\text{Ta}_{0.5}\text{Ti}_{1.5}$ .....	68
<b>6 Conclusions</b> .....	<b>73</b>
<b>7 Suggestions for future works</b> .....	<b>75</b>
<b>8 Acknowledgements</b> .....	<b>77</b>
<b>References</b> .....	<b>79</b>





## **1 Introduction**

There is a constant need for structural materials possessing excellent properties including strength, ductility, thermal stability and toughness. In this regard, some of the well-known commercial alloys include aluminum alloys, titanium alloys, high-speed steels and nickel (Ni)-based superalloys. Among these alloys, Ni-based superalloys have gained significant attention because of their ability to bear structural load for high-temperature applications. Important characteristic of Ni-based alloys include their high strength above 600 °C, which can be maintained up to 90 % of the melting temperature i.e., 1150 °C. Some other critical features include good fracture toughness and room temperature ductility, favorable creep and fatigue behavior, and high microstructural stability, thus making them materials of choice for high temperature applications such as turbine engine blades. Currently, Ni-based alloys can function up to 1150 °C without any cooling, which is their highest operating temperature. Some of the hottest areas of turbine engine can even reach up to 1500 °C, but complex cooling systems and thermal barrier coatings are incorporated into the blades. These add-ons have resulted in an increased inefficiency losses as a large amount of power produced is continuously invested on the cooling of turbine blades during operation. Studies have shown that the development trend of Ni-based alloys for gas turbine engines, has deviated from the ideal performance over a number of years with the increased inefficiency losses, as determined from Fig. 1(a) by the correlation between specific core power against turbine inlet temperature [1].

The current state of development for high temperature materials is staggering and requires alternate development route. Nevertheless, it also encourage researchers and material scientists to look for new materials which can replace the current state-of-the-art materials, i.e., Ni-based superalloys. For reader's information, the typical microstructure of Ni-based superalloy with

cuboidal ordered face centered cubic (fcc) precipitates surrounded by a disordered fcc matrix is also shown in Fig. 1 (b) [2].

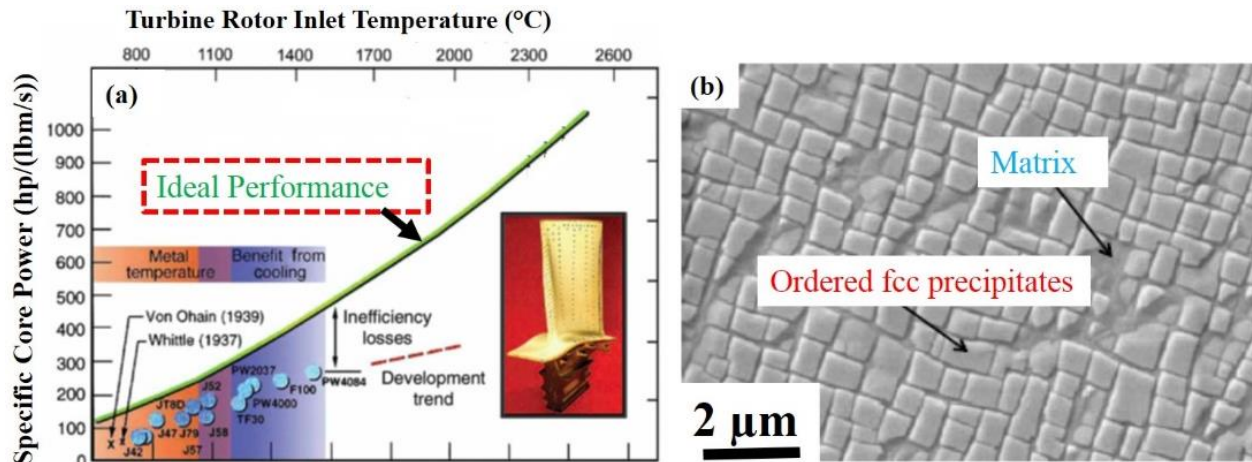


**Figure 1: Specific core power versus turbine rotor inlet temperature (a); typical Ni-based alloy microstructure (b), published and edited with permission from Elsevier B.V. and Springer Singapore.**

Significant efforts are underway to develop new materials that can function at temperatures higher than the current capacity, considering the performance of a Carnot engine is directly linked to the homologous working temperature. Therefore, to minimize inefficiency is to introduce new ultrahigh temperature structural materials superior than current nickel-based superalloys which can function at  $\geq 1300$  °C without any necessary cooling [3].

### 1.1 Aim for this study

Among various efforts to address the current challenge for inefficiency losses, one of the leading research direction in materials science is to design materials that possess strength and stiffness at the highest achievable temperatures. In this regard, one particular reported guideline for alternate materials is the Johnson relation, which suggests that the melting temperature ( $T_m$ ) of the material should be above 2500 °C in order to be used as turbine blades, without any protection from

coatings and cooling [4].  $T_m$  is indeed one of the most critical and useful structure-insensitive parameter, since it defines the thermal region where materials can remain solid.  $T_m$  is also related to the stiffness of a material with direct link to the elastic moduli [5]. Another important property that can be derived from  $T_m$  is the creep resistance, which generally improves with the increasing  $T_m$ , and is extremely important for applications such as turbine blades, as they are constantly subjected to stresses by centrifugal forces during operation. Until now, only a limited number of alternate materials are known which can fulfill the requirements of higher  $T_m$ . The list includes materials such as intermetallic compounds, ceramics and refractory metals and alloys. Apart from  $T_m$ , another major concern for materials operating at high temperatures is the oxidation resistance, related to chemical activity. Generally, intermetallic compounds and ceramics possess good oxidation resistance, but they suffer from low room-temperature ductility and toughness, hence limiting their usage. Similarly, alloys containing refractory metals, for example, Mo-Si-B alloys and niobium alloys, seems promising but, there are challenges related to oxidation resistance and processing [6]. Recently, high-entropy alloys (HEAs) have gained significant attention due to their impressive strength, softening resistance, hardness, wear and corrosion resistance [7-9]. They mostly form simple solid solutions with fcc and body-centered cubic (bcc) crystal structures. Generally, fcc-type HEAs are soft and malleable [10]. The bcc-type HEAs have high strength but are usually brittle. Senkov et al. [11-16] has reported a series of bcc refractory HEAs (RHEAs), with high compressive yield strength and hardness, but most of these alloys only show low compressive strain at room temperature. It is well known that tensile properties are more important for engineering and structural application rather than compressive properties. Therefore, searching for new HEAs with optimized strength and tensile ductility, that can function at both room and high temperature, is still a challenge, and it constitutes the main aim for this study.

## 1.2 Research goals

HEAs are only 14 years old and have already attracted lots of new ideas to explore the enormous compositional space provided by them. HEAs usually form simple solid solutions, but in some cases unwanted secondary phases particularly intermetallic compounds, and even the amorphous phases are also formed, thus affecting their properties [17-19]. Therefore, the main challenge that HEAs are currently facing is associated with the effective alloy design which can provide information to choose suitable constituent elements, resulting in desired phase constitution and microstructure, and in the end, optimum properties. Here, in this work, it all started by introducing new and improved guidelines to separate the formation of solid solutions and intermetallic compounds by more accurately locating the solid solubility limit. Later, the mechanism and route for developing intrinsically ductile RHEAs, with single phase bcc solid solution was proposed. Thermomechanical treatments were applied to further optimize the mechanical properties of ductile RHEAs. Later on, high temperature oxidation resistance studies of RHEAs were also carried out to further promote the development of ductile RHEAs with balanced high-temperature oxidation resistance and room-temperature ductility, since the ultimate aim of this work is to develop ductile materials for ultrahigh-temperature applications. Efforts were also focused on improving the oxidation resistance through aluminizing. Figure 2 outlines the main goals for the current study:

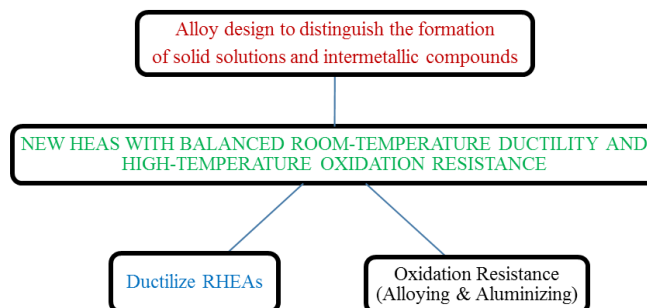


**Figure 2 Proposed outline with the research goals for current work.**





## 2 High-entropy alloys

### 2.1 Introduction of high-entropy alloys

High-entropy alloys (HEAs), a novel alloying concept in physical metallurgy, contain at least four principal elements [20, 21]. HEAs have gained considerable interest because of their potential in structural and functional applications [22]. Depending on the alloy compositions, HEAs can form simple solid solutions, such as fcc and bcc phases. Thermodynamically, it is well established that a system tries to minimize its Gibbs free energy ( $\Delta G_{\text{mix}}$ ) to achieve a stable or metastable state. Enthalpy of mixing ( $\Delta H_{\text{mix}}$ ) and total mixing entropy ( $\Delta S_{\text{mix}}$ ) are related to Gibbs free energy for a given temperature (T), expressed in Kelvin, with the relation shown by Equation 1 [23].

$$\Delta G_{\text{mix}} = \Delta H_{\text{mix}} - T\Delta S_{\text{mix}} \quad \text{Eq. 1}$$

Decreasing enthalpy of mixing or increasing mixing entropy can decrease the Gibbs free energy. For alloys containing multiple elements, there can be plenty of competing phases depending on the constituent elements, but the phase with the lowest  $\Delta G_{\text{mix}}$  is principally in the equilibrium state. The competition between  $\Delta H_{\text{mix}}$  and  $T\Delta S_{\text{mix}}$  basically determines the phase formation. At higher temperatures, the term  $T\Delta S_{\text{mix}}$  becomes dominant and promotes the formation of solid solutions.  $\Delta S_{\text{mix}}$  has four major contributions and is equal to the sum of contributions from the configurational (for e.g. different-sized atoms) and non-configurational (vibrational, magnetic dipole, and electronic randomness) components [24]. The reported literature on HEAs emphasizes that the highest contribution of  $\Delta S_{\text{mix}}$  comes from configurational entropy, similar to the ideal solutions [25]. Configurational entropy is higher in HEAs in comparison to that in conventional alloys, which usually have one or at most two principal elements [26]. From statistical thermodynamics, Boltzmann's equation can determine the configurational entropy of a

system, comprising of N components [27]. Ideal configurational entropy per mole for a random solid solution with N-components, in which the *i*th component has a mole fraction,  $c_i$ , is given in Equation 2 [28]. Entropy would reach a maximum when the alloy is in the equiatomic ratio, and is expressed in Equation 3, where R is the gas constant 8.314 J/(Kmol).

$$\Delta S_{mix} = -R \sum_{i=1}^N c_i \ln c_i \quad \text{Eq. 2}$$

$$\Delta S_{mix} = R \ln N \quad \text{Eq. 3}$$

The configurational entropy increases as the number of elements increases. Table 1 lists the configurational entropies of equiatomic alloys in relation to the gas constant, R, obtained using Equation 3.

**Table 1: Configurational entropies in terms of R with up to 13 constituent elements for equiatomic alloys [29].**

N	1	2	3	4	5	6	7	8	9	10	11	12	13
$\Delta S_{mix}/R$	0	0.69	1.1	1.39	1.61	1.79	1.95	2.08	2.2	2.3	2.4	2.49	2.57

It is noted that the configurational entropy of alloys with four elements under ideal circumstances is 1.39 R. Further increasing the number of elements gives only gradual contribution to  $\Delta S_{mix}$ . Nevertheless, there are many studies investigating those HEAs with a large number of N, to study whether a higher configuration entropy can tend to keep a single-phase solid solution at ambient temperature. However, no single value for  $\Delta S_{mix}$  could be agreed upon that can allow to distinguish HEAs from conventional alloys [24].

## 2.2 Key characteristics of HEAs

Current knowledge of physical metallurgy is mostly based upon the outcome obtained from conventional alloys, but HEAs are different compared to conventional alloys, hence need to be

investigated carefully. Some of the key features affecting the properties and microstructure, widely used to describe HEAs include : a) lattice distortion, and b) high-entropy effect [20]. Fig. 4 shows the influence of these properties upon the physical metallurgy of HEAs, and how these features can be utilized to control the development of HEAs. Processing, crystal structure, alloying composition and microstructure are correlated to kinetics, thermodynamics and deformation theory [30].

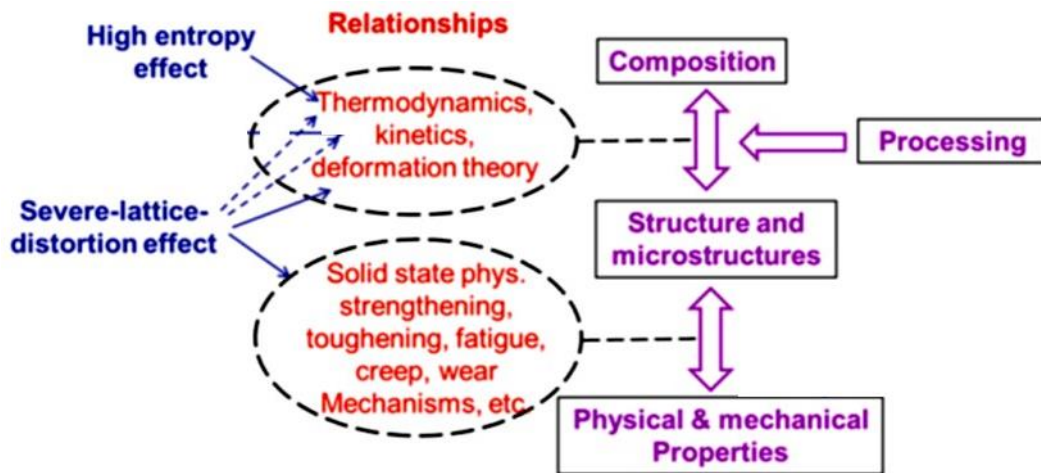


**Figure 4: Influence of HEAs key characteristics on their physical metallurgy [30], published and edited with permission from Springer.**

High-entropy effect is the core principle of HEAs, indicating increased  $\Delta S_{\text{mix}}$  can stabilize the formation of simpler structures comprising of solid solutions, over competing secondary/intermetallic compounds. This idea has been confirmed by one of the most widely studied HEA with the equiatomic composition, CoCrFeMnNi, a simple single phase fcc solid solution in the as-cast state [31]. Another reported system is the equiatomic AlCoCrCuFeNi system, which contains a mixture of fcc and bcc structures. With the addition of Al in the  $\text{Al}_x\text{CoCrCuFeNi}$  HEA system, the crystal structure shifts from single fcc phase, to two phases, fcc plus bcc solid solutions, and eventually fully bcc phase [32]. Similarly, refractory

HfNbTaTiZr HEA forms simple bcc phase in the as-cast state and homogenized state without any formation of secondary phases [33]. All of these HEA systems indicate that the contribution from higher entropy can limit the formation of competing secondary intermetallic compounds and elemental phases, thus promoting the formation of solid solutions. To further reveal the role of high-entropy, Fig. 5 shows X-ray diffraction (XRD) patterns of an equimolar HEA series of AlCoCrCuFeNiSi in the as-cast condition, starting from the binary alloy up to the septenary alloy [34]. Despite increasing number of elements, simple solid-solutions comprising of fcc and bcc phases were formed, and high-entropy inhibited the formation of intermetallic compounds. For all alloys in this series, there is no principal element, and all atoms distribute randomly within the crystal lattice.

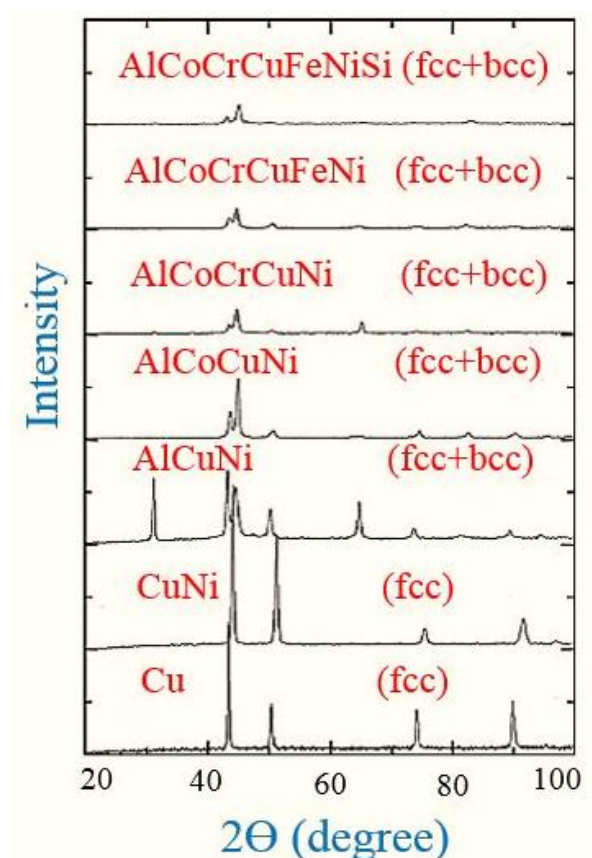


**Figure 5: XRD of an equimolar HEA series of AlCoCrCuFeNiSi in the as-cast condition, with alloys containing two up to seven elements [34], published and edited with permission from Elsevier B.V.**

Another feature of interest for HEAs is their large lattice distortion, originating mainly from the large atomic size mismatch among different constituent alloying elements, which finds correlation to deformation theory, kinetics, thermodynamics, mechanical properties associated with material strengthening, fatigue, creep, etc. In comparison, conventional alloys contain rather similar kind of atoms in majority as their neighbors, which results in lower lattice distortion. The displacement at each lattice site depends on the atom occupying that site and the types of atoms in the local environment. Atoms with varying sizes can cause local uncertainty in their respective atomic positions, resulting in extra configurational entropy. This uncertainty in atomic positions becomes more significant with increasing atomic size differences and concentrations. There are some experimental studies which have reported the lowering of intensity of X-ray diffraction peaks, reduced electrical and thermal conductivity, and solid solution hardening due to severe lattice distortion in HEAs [20, 35]. Although, these studies seem quite interesting, more investigations are required to gain more confidence with respect to such claims. A schematic illustration of a perfect bcc lattice for Cr, in comparison to a distorted lattice for AlCoCrFeNiTi<sub>x</sub> with atoms randomly distributed, is shown in Fig. 6 [36].

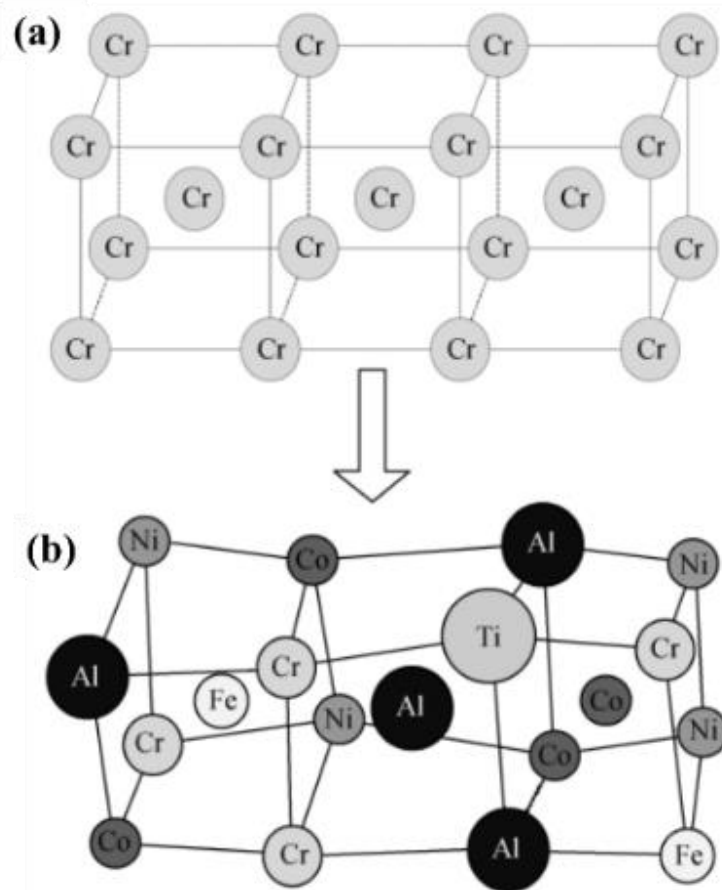


**Figure 6: Schematic of a bcc structure: (a) an ideal Chromium (Cr) lattice; (b) distorted lattice containing different-sized atoms which are randomly distributed in the crystal lattice [36], published with permission from SP Science in China Press.**

### 3 Alloy design and current challenges to HEAs

HEAs are promising for new high-temperature materials because of their compositional flexibility, which can allow to enhance the corrosion and oxidation resistance. Slow diffusion kinetics and softening resistance at elevated temperatures also gives them advantage for such applications. However, it appears they still have a long way to go in replacing current high-temperature materials. The biggest challenge for HEAs in terms of their utilization in engineering applications is the trade-off between strength and ductility, strongly linked to the choice of constituent elements to achieve desired phase constitution and properties. Alloy design can also include other properties as well, for example replacing heavier and expensive elements with lighter and rather cheaper elements [15, 16]. HEAs with fcc crystal structure are known to be ductile, but their strength is usually low, while bcc HEAs are much stronger but quite often high strength comes along with brittleness, especially during tensile loading. Alloy design can be manipulated using valence electron concentration (*VEC*), where addition of elements with higher *VEC* favour the formation of fcc solid solutions, while adding an element with lower *VEC* promotes bcc solid solutions formation. Needless to say, alloy design is directly related to mechanical properties [37]. However, the *VEC* rule is only valid when solid solutions are formed. HEAs can form single-phase solid solution, but it is not always that single-phase solid solution can form in HEAs, as other phase constitutions like intermetallic compounds or even the amorphous phases can occur [17, 38-40].

Despite knowingly that high mixing entropy promotes the formation of solid solutions in HEAs, however, it is not the only dominant factor to decide the phase formation. Other prominent factors include mixing enthalpy, atomic size difference and electronegativity. Current alloy design strategies for HEAs to control the formation of solid solutions, intermetallics and amorphous phases are essentially derived from binary solid solutions and metallic glasses. They make use of

parameters such as: electronegativity, atomic size mismatch, and the mixing enthalpy. In this regard, one particular approach comprising of two-parameters i.e.,  $\delta - \Delta H_{mix}$ , is widely reported to control the formation of solid solutions in HEAs [19, 38], where  $\delta$  is the atomic size mismatch and  $\Delta H_{mix}$  is the averaged mixing enthalpy of alloys, as defined in Equations 4 and 5.

$$\delta = \sqrt{\sum_{i=1}^n c_i \left(1 - \frac{r_i}{\sum_{j=1}^n c_j r_j}\right)^2} \quad \text{Eq. 4}$$

$$\Delta H_{mix} = \sum_{i=1, j>i}^n 4\Delta H_{AB}^{mix} c_i c_j, \Delta H_{AB}^{mix} \quad \text{Eq. 5}$$

Where  $n$  is the number of alloying elements,  $c_i$  and  $c_j$  is the atomic percentage for the  $i$ th and  $j$ th element, and  $r_i$  or  $r_j$  are the atomic radii for the  $i$ th or  $j$ th element respectively, and  $\Delta H_{AB}^{mix}$  is the enthalpy of mixing for the binary equiatomic AB alloys. Solid solutions form at  $\delta \leq 6.6$  and  $\Delta H_{mix}$  is not notably negative, usually in the range  $-11.6 \text{ KJ/mol} \leq \Delta H_{mix} < -3.2 \text{ KJ/mol}$ . Figure 7 shows the result from the available experimental reported data on the phase selection in HEAs, using the two parameters  $\delta$  and  $\Delta H_{mix}$  [19].

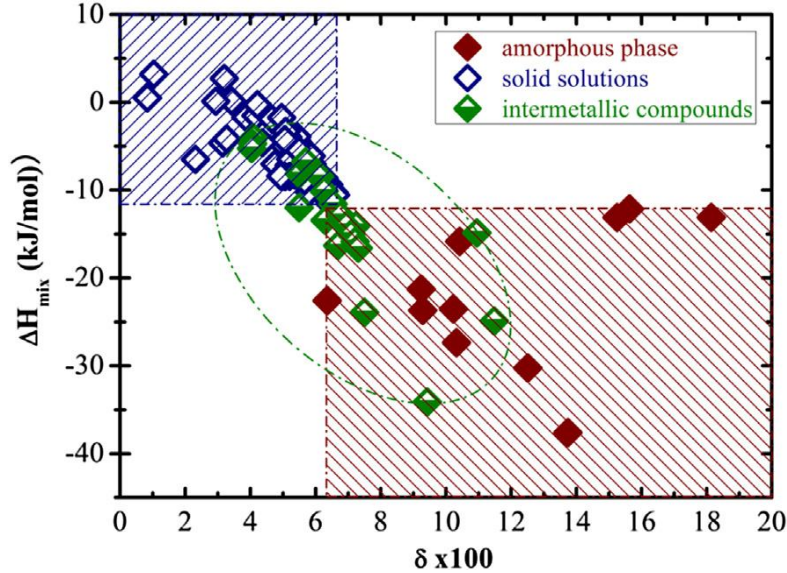


**Figure 7: Phase selection in high entropy alloys using  $\delta - \Delta H_{mix}$  with coinciding regions where solid solutions and intermetallics exist as well as amorphous phases and intermetallics [41], published with permission from Elsevier B.V.**

The dotted regions highlight different areas forming solid solutions, intermetallic compounds and the amorphous phase. There exists an overlapping region in the two-dimensional  $\delta - \Delta H_{mix}$  map where both solid solutions and intermetallic exist, and also both, amorphous phases and intermetallics exist. Such an overlapping using  $\delta - \Delta H_{mix}$  fails to distinguish accurately between solid solutions and intermetallic compounds, and is hence not desirable and motivates to use an alternative alloy design criteria, especially to control the formation of intermetallic compounds from the mechanical properties perspective. Intermetallic compounds have been known to play a critical role in either strengthening or embrittling of alloys [42]. Efforts are usually directed to avoid the formation of intermetallic compounds, particularly topologically closed-pack (TCP) phases and geometrically closed-pack (GCP) phases, such as  $\sigma$  phase, R phase, A15 phase,  $\mu$  phase,  $\chi$  phase, Laves phase and  $\eta$  phase. Such phases are usually undesirable and brittle in nature, and tend to appear during service. Structurally, TCP phases have close-packed atoms in layers, which are divided by comparatively large interatomic distances, while GCP are close-packed in all directions. Such phases are usually desirable and brittle in nature, and tend to appear during service. Therefore, the capability to differentiate accurately between the formation of solid solutions and intermetallic compounds such as TCP and GCP phases, is still a challenge, and requires further attention.

### **3.1 The $Md$ parameter**

Addressing the need to explore alternative alloy design opportunities with better capability to separate the formation of solid solutions and intermetallic compounds, we have determined the prospect of utilizing the parameter  $Md$ , the average d orbitals energy level of the constituent transition metals in HEAs, to predict the phase boundaries between solid solutions and TCP/GCP phases [43].  $Md$  has been a useful parameter to predict the solid solubility limit in transition-

metal-based alloys such as nickel-based, cobalt-based and iron-based alloys. Since HEAs are mostly composed of transition metals,  $Md$  could also be applicable to HEAs. The parameter  $Md$  and its potential to determine the solid solubility was introduced by Morinaga et al. [43]. It utilizes cluster calculations to identify the d-orbital energy level of transition elements, within a specific base metal X. For example, in the case of a pure Fe cluster, the levels of  $8e_g$  to  $16t_{2g}$  emerge largely from the Fe 3d orbitals, and establish the Fe 3d band where the Fermi energy level is present [44]. When pure Fe is alloyed, new energy levels mainly due to the d-orbitals of the alloying transition metal emerge above the Fermi energy level. These energy levels vary orderly as per the elemental sequence in the periodic table. The average energy of two such d-orbital levels, i.e.,  $e_g$  and  $t_{2g}$ , is  $Md$ . Similarly, cluster calculations are also extended to other metals such as fcc Ni, and are calculated in a similar manner as mentioned earlier for Fe cluster.  $Md$  values of  $Ni_3Al$  are used for Ni-based superalloys, since the lattice parameter of  $Ni_3Al$  is similar to that of Ni. For  $Ni_3Al$ , the levels of  $13a_{1g}$  to  $15e_g$  are predominantly originated from Ni 3d orbitals, i.e., where the Fermi level lies as shown by arrows in Fig. 8. With the addition of transition elements to  $Ni_3Al$ , new energy levels due to the d orbitals of alloying elements appear above the Fermi level.  $16e_g$  and  $14t_{2g}$  are shown with dotted levels in Fig. 8, and the average energy of two such d-orbital levels correspond to  $Md$ .

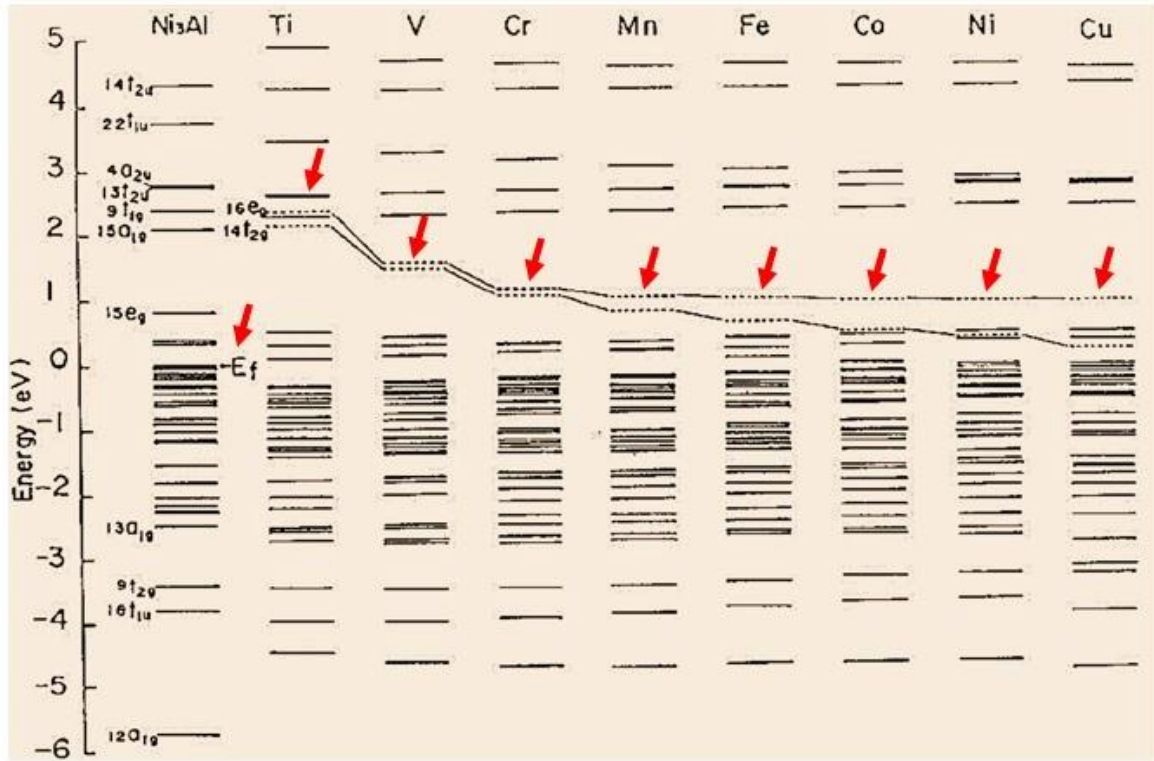


**Figure 8: Energy level structures of pure and alloyed Ni<sub>3</sub>Al with 3d transition metals [45], published and edited with permission from Springer Science.**

Some of the  $Md$  values, for various transition metals (M) in Ni, used by Morinaga et al. to determine the solid solubility in Ni-based superalloys are listed in Table 2 [46]. Al and Si are added as non-transition metals, and their  $Md$  are empirical values and obtained from interpolation [44].

**Table 2: List of  $Md$  values for common transition metals  $M$  in fcc Ni used to determine solid solubility in fcc alloys [46].**

	<b>Element <math>M</math> in fcc Ni</b>	<b><math>Md</math> (eV)</b>
3d	Ti	2.271
	V	1.543
	Cr	1.142
	Mn	0.957
	Fe	0.858
	Co	0.777
	Ni	0.717
	Cu	0.615
4d	Zr	2.944
	Nb	2.117
	Mo	1.55
5d	Hf	3.02
	Ta	2.224
	W	1.655
	Re	1.267
others	Al	1.9
	Si	1.9

The average value of  $Md$  for alloys is defined by taking the compositional average, as given by Equation 6:

$$Md = \sum_{i=1}^n c_i (Md)_i \quad \text{Eq. 6}$$

The  $Md$  levels are related to the electronegativity and the atomic radius of elements in a way that as  $Md$  levels increase, the electronegativity decreases, but increases again with increasing atomic

radius of the element [44]. When  $Md$  increases above a certain limit, the phase instability will occur and secondary phase will appear. A single parameter, the critical  $Md$  value was found to be able to determine the solubility limit of the terminal solid solution. The critical  $Md$  value also depends on the type of the secondary phase. To determine the impact of the parameter  $Md$  on solid solubility among solid solutions and TCP/GCP phases in HEAs, we have inspected a considerable number of HEA systems with reportedly fcc solid solutions and fcc solid solutions plus TCP/GCP phases ( $\sigma$  phase, R phase,  $\mu$  phase and Laves phase/ $\eta$  phase), as shown in Table 3. The average value of  $Md$  for alloys is also given (paper I).

**Table 3: Phase constitutions in fcc structured HEAs containing 3d and 4d transition metals, and their d-orbital energy level,  $Md$ .**

Alloy system	Phase	$Md$	Reference
CoCrCuFeNi	fcc	0.82	[32]
CoCrCu <sub>0.5</sub> FeNi	fcc	0.84	[47]
CoCrFeMnNi	fcc	0.89	[8]
CoCrFeNi	fcc	0.87	[25]
CoCrCuFeMnNi	fcc	0.84	[8]
Al <sub>0.25</sub> CoCrCu <sub>0.75</sub> FeNi	fcc	0.88	[48]
CoCrFeNiMo <sub>0.1</sub>	fcc	0.89	[49]
CoCrFeNiMo <sub>0.3</sub>	fcc+ $\sigma$	0.92	[50]
CoCrFeNiTi <sub>0.5</sub>	fcc+ $\sigma$ +Laves+R	1.02	[51]
CoCrCuFeNiTi <sub>0.8</sub>	fcc+Laves	1.02	[52]
CoCrCuFeNiTi	fcc+Laves	1.06	[52]
Co <sub>1.5</sub> CrFeNi <sub>1.5</sub> Ti <sub>0.5</sub>	fcc+ $\eta$	0.97	[53]
Al <sub>0.3</sub> CoCrFeNiTi <sub>0.1</sub>	fcc+ $\eta$	0.97	[54]

### 3.2 *Md* and Thermo-Calc

Theoretical or empirical approaches to predict the solid solubility, and to be able to control the formation of intermetallic compounds are of prime interest both scientifically and from practical engineering applications perspective. In the materials science field, unification of the CALPHAD approach to experimental results has gained a lot of interest in identifying phase diagrams for a given alloy system at particular temperatures. CALPHAD is the abbreviation for CALculation of PHase Diagrams and combines phase diagram and thermodynamics. It can allow to identify the type of phases formed, their respective compositions, thermodynamic property information and transformation temperatures. The CALPHAD approach is based on the formulation of thermodynamic functions, established from the experimental data and derived from thermodynamic properties and phase diagrams [55, 56]. Outcome generated from these empirical and semi-empirical functions and their correlating fitting parameters are referred to as databases. For HEAs, the TCHEA1 (newer version of TCHEA2 commercially available now) database is created based on the TCNI database, preferably used for Ni-based alloys. TCHEA1 contains the entire range of binary systems and most of the ternary systems with all probable phases. During the course of this work, the *Md* concept was also validated by comparing with the phase diagram for  $\text{CoCrFeNiZr}_x$  calculated using the TCHEA1 database. The aim was to gauge Zr (4d transition metals) solid solubility in the fcc structured HEAs, CoCrFeNi. Zr was added with varying amount to improve the solid solution strengthening effect due to the dissolution of Zr with larger atomic radius element within CoCrFeNi. Later on, experiments were also carried out to determine the phase constitution of  $\text{CoCrFeNiZr}_x$  alloys judging mainly from the XRD and microstructure (paper II).

### 3.3 *Md* and mechanical properties

It is important to mention here that the ultimate point of interest of the *Md* concept is to address the strength-ductility trade-off in HEAs by correlating with the type of phase constitutions. In this regard, the *Md* concept can be extended to not only predicting the solid solubility, but also utilizing it to design HEAs with exceptional mechanical properties, especially for those HEAs which contain more than one single solid solution phase.  $\text{Co}_{35}\text{Cr}_{15}\text{Fe}_{20}\text{Mo}_{10}\text{Ni}_{20}$  is one such example which comprises of two phases i.e., fcc solid solution and secondary Mo-rich  $\mu$  phase. Despite the presence of the  $\mu$  phase, this HEA showed exceptional strength-ductility combination due to nanotwinning and the significant solid solution strengthening role of Mo [57]. This HEA was ductile in the as-cast state, and subsequent thermo-mechanical treatments helped to significantly improve both yield and ultimate strengths, as shown in Fig. 9. Therefore, working along this line, *Md* can help to identify those HEAs which can form secondary intermetallics in combination with optimum mechanical properties.

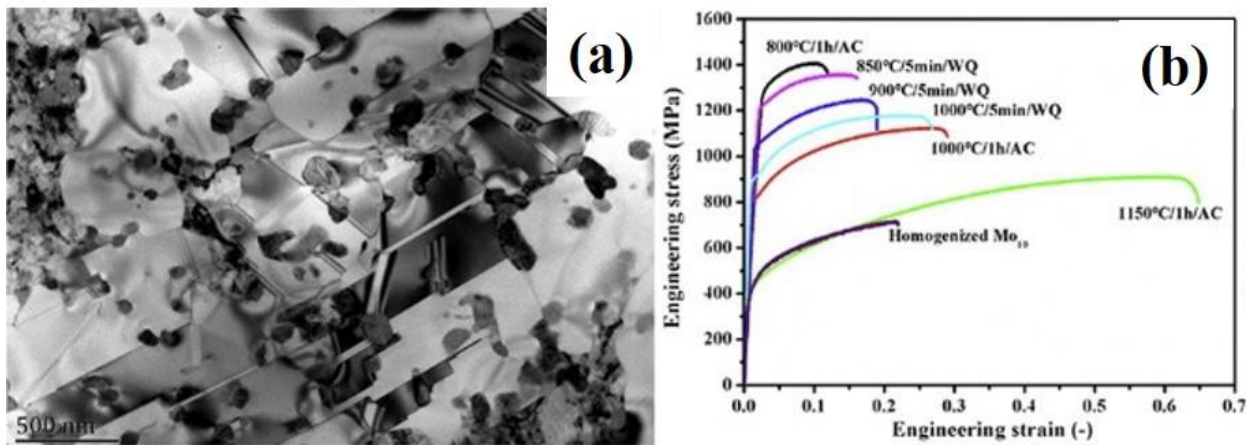


**Figure 9: A TEM microstructure of the  $\text{Cr}_{15}\text{Fe}_{20}\text{Co}_{35}\text{Ni}_{20}\text{Mo}_{10}$  HEA comprising of thin bands representing annealing twins, while black regions correspond to  $\mu$  phases (a); room-temperature engineering stress-strain curves for the thermomechanically treated  $\text{Cr}_{15}\text{Fe}_{20}\text{Co}_{35}\text{Ni}_{20}\text{Mo}_{10}$  HEA (b), published with permission from Institute for Scientific Information.**

### 3.4 Mechanical properties of HEAs

Transition metals are most commonly used to synthesize HEAs. The atomic radii for elements such as Fe, Ni, Cr, Co and Cu are quite similar, and mixing enthalpies among them are insignificantly negative. HEAs consisting of such elements have the tendency to form simple fcc solid solutions, as reported by Chen et al., but they are accompanied with low mechanical strength, which is not attractive for applications. Aluminium was added into a CoCrCuFeNi system, and with the increase in Al, the single phase fcc solid solution transformed to a mixture of fcc and bcc solid solutions. The hardness values also increased with increasing Al content, which can be related to the increase in lattice distortion and the formation of the harder bcc phase [58]. Wang et al. has reported that the addition of Al in the CoCrCuFeNiTi<sub>x</sub> system with simple fcc solid solution formation, while the amount of Ti was kept lower, but secondary phases started to appear as Ti content was increased [52]. Chen et al. investigated the properties of Al<sub>0.5</sub>CoCrCuFeNiTi<sub>x</sub> by varying Ti content [59]. Simple fcc phase appeared with lower Ti, but as Ti content was increased, a mixture of fcc and bcc phases was formed. By further increasing Ti, Ti<sub>2</sub>Ni-like phase (TL) structure and sigma ( $\sigma$ ) phases appeared. Having Ti  $\geq$  1.2 atomic portion,  $\sigma$  phase disappeared, but the mixed fcc, bcc and TL phases were still present. Hardness of the alloy system increased from HV 225 to HV 770 with the increase in the amount of Ti. Change of mechanical strength in this HEA system resulted mainly from the phase transformation from fcc to bcc, and also from the precipitation of inter-metallic compounds, such as  $\sigma$  phase and TL phases. Phase constitution and hardness for Al<sub>x</sub>CoCrCuFeNi and Al<sub>0.5</sub>CoCrCuFeNiTi<sub>x</sub> are shown in Table 4:

**Table 4: Phase constitution and hardness for  $\text{Al}_x\text{CoCrCuFeNi}$  and  $\text{Al}_{0.5}\text{CoCrCuFeNiTi}_x$  system with increase in Al content and Ti content respectively [58, 59].**

Alloy	Phase constitution	Hardness	Reference
CoCrCuFeNi	fcc	133	[58]
$\text{Al}_{0.3}\text{CoCrCuFeNi}$	fcc	180	[58]
$\text{Al}_{0.5}\text{CoCrCuFeNi}$	fcc	208	[58]
$\text{Al}_{0.8}\text{CoCrCuFeNi}$	fcc+bcc	271	[58]
AlCoCrCuFeNi	fcc+bcc	406	[58]
$\text{Al}_{0.5}\text{CoCrCuFeNiTi}_{0.2}$	fcc	275	[59]
$\text{Al}_{0.5}\text{CoCrCuFeNiTi}_{0.4}$	fcc+bcc	325	[59]
$\text{Al}_{0.5}\text{CoCrCuFeNiTi}_{0.6}$	fcc+bcc	460	[59]
$\text{Al}_{0.5}\text{CoCrCuFeNiTi}_{0.8}$	fcc+bcc+sigma phase	590	[59]
$\text{Al}_{0.5}\text{CoCrCuFeNiTi}_1$	fcc+bcc+sigma phase	630	[59]
$\text{Al}_{0.5}\text{CoCrCuFeNiTi}_{1.2}$	fcc+bcc+sigma phase+TL	650	[59]
$\text{Al}_{0.5}\text{CoCrCuFeNiTi}_{1.4}$	fcc+bcc+TL	660	[59]
$\text{Al}_{0.5}\text{CoCrCuFeNiTi}_{1.6}$	fcc+bcc+TL	670	[59]
$\text{Al}_{0.5}\text{CoCrCuFeNiTi}_{1.8}$	fcc+bcc+TL	680	[59]
$\text{Al}_{0.5}\text{CoCrCuFeNiTi}_2$	fcc+bcc+TL	700	[59]

Ma et al. [60] studied the Nb alloying effect, on AlCoCrFeNb<sub>x</sub>Ni HEAs system and reported the formation of bcc solid solution phase together with ordered Laves phase of (CoCr)Nb-type. The microstructures of the alloy changed from hypoeutectic to hypereutectic, with compressive yield

strength and Vickers hardness going through a linear increase with the addition of Nb content, as shown in Table 5.

**Table 5: Mechanical properties under compression and Vickers hardness of as-cast AlCoCrFeNbxNi (where x = 0.1, 0.25, and 0.5) alloys [60].**

Alloy	$\sigma_{0.2}$ (MPa)	$\sigma_{max}$ (MPa)	$\epsilon_p$ (%)	HV
AlCoCrFeNb <sub>0.1</sub> Ni	1641	3285	17.2	569
AlCoCrFeNb <sub>0.25</sub> Ni	1959	3008	10.5	669
AlCoCrFeNb <sub>0.5</sub> Ni	2473	3170	4.1	747

Results from compression testing shows that the yield strength substantially increased from 1641 MPa to 2473 MPa, while the plastic strain significantly decreased from 17.2 % to 4.1%, which is due to the Nb addition. It is also found that the plasticity of the alloys is getting progressively worse as a result of the increasing amount of the brittle Laves phase.

### 3.4.1 Properties under tensile testing

Considerable number of data is available for tensile testing of HEAs. Reported HEAs are mostly comprising of 3d transition metals mixed with Al, and some typical tensile properties are mentioned in Table 6. Although direct comparison of data is difficult here due to differences in the type and concentration of principal elements and phase compositions, general observations can still be made. Al<sub>0.3</sub>CoCrFeNi (7.0 at.% Al) and Al<sub>0.5</sub>CoCrCu<sub>0.5</sub>FeNi<sub>2</sub> (8.1 at.% Al) are the alloys with the lowest Al concentration and similar phase constitution. Their microstructures contain primarily fcc and L1<sub>2</sub> nanoprecipitates (cP4, AuCu<sub>3</sub> prototype), and  $\sigma_{UTS}$  is rather similar for both alloys. Al<sub>0.5</sub>CoCrCuFeNi (18.3 at.% Cu) contains the highest Cu concentration of alloys amongst the reported HEAs in the table and consists of two fcc phases with a primary fcc and secondary Cu-rich fcc phase. The maximum  $\sigma_{UTS}$  it could achieve is around 707 MPa with

elongation to failure of 19 %. With the increase in Al content as in AlCoCrCuFeNi (16.7 at.% Al), it is noted that although  $\sigma_y$  and  $\sigma_{UTS}$  are the highest, the elongation to failure is the least reported (0.2 %) and the material is brittle. Therefore, both strength and ductility need to be optimized to make them attractive for real applications.

**Table 6: Mechanical properties under tensile testing for different as-cast HEAs.**

Alloy	Phase constitution	$\sigma_y$ (MPa)	$\sigma_{UTS}$ (MPa)	$\epsilon$ (%)	Reference
Al <sub>0.3</sub> CoCrFeNi	fcc + L1 <sub>2</sub>	224 ± 51	434 ± 94	48 ± 10	[61]
Al <sub>0.5</sub> CoCrCu <sub>0.5</sub> FeNi <sub>2</sub>	fcc + L1 <sub>2</sub>	357	459	9	[62]
Al <sub>0.5</sub> CoCrCuFeNi	fcc + fcc	360	707	19	[63]
AlCoCrCuFeNi	bcc+fcc+ B2 + L1 <sub>2</sub>	790	790	0.2	[64]

### 3.4.2 Beyond tensile properties

Within the scope of mechanical properties, some limited studies on fracture toughness and fatigue behaviour of HEAs are also reported. Most extensive fracture toughness studies for HEAs are conducted on CoCrFeMnNi (single phase fcc structured HEA), with fracture toughness values surpassing 200 MPa.m<sup>1/2</sup> and tensile strengths over 1 GPa [65]. These impressive fracture toughness of CoCrFeMnNi was related to 100 % ductile fracture because of the microvoid coalescence. Mechanical properties were also exceptional at cryogenic temperatures down to 77 K. The superior properties are ascribed to a shift in the deformation mechanism from planar-slip dislocation at room temperature to mechanical nanotwinning with the decreasing

temperature, which results in a steady strain hardening by suppressing plastic instability. Regarding the fatigue behavior of HEAs,  $\text{Al}_{0.5}\text{CoCrCuFeNi}$  consisting of FCC and  $\text{L}_{12}$  phases, after four-point bending fatigue shows that the alloy has a fatigue endurance limit between 540 and 945 MPa [66]. The ratio of endurance limit and UTS is between 0.402 and 0.703 and can be favorably compared with steels, aluminium, titanium alloys and nickel alloys. However, further studies to achieve better knowledge related to the fatigue behaviour are required.

### **3.5 Refractory high-entropy alloys (RHEAs)**

Refractory metals refer to W, Mo, Ta and Nb, and alloys, comprising of these metals are critical for high temperature and high strength applications, also known as heat-resistant alloys. Within the category of refractory metals, there is also a wider definition of refractory metals, including elements such as Ti, Zr, Hf, V, Cr, Ru, Os, Rh, and Ir. Although, the elements in this extended list also possess high  $T_m$ , but not as high as the principal refractory metals. The crystal structure of refractory metals is related to their position in the periodic table and can be determined by their electronic structure. Group IV (Ti, Zr, Hf) are polymorphic with the low temperature structure of metals consisting of hexagonal close-packed (hcp) lattice, while the bcc lattice becomes stable at high-temperature. Metals of group V (V, Nb, Ta) and group VI (Cr, Mo, W) are monomorphic with bcc lattice, while Re, Ru, Os have a hcp lattice [67]. Some of the key properties such as melting point and density ( $\rho$ ) are shown in Table 7 where Ti is the lightest metal as per density and Ir is the heaviest.

**Table 7: Melting point and density of refractory elements [68].**

Element	Melting point (° C)	$\rho$ (g/cm <sup>3</sup> )
Titanium, Ti	1668	4.507
Zirconium, Zr	1855	6.511
Hafnium, Hf	2233	13.31
Vanadium, V	1910	6.11
Niobium, Nb	2477	8.57
Tantalum, Ta	3017	16.65
Chromium, Cr	1907	7.14
Molybdenum, Mo	2623	10.28
Tungsten, W	3422	19.25
Rhenium, Re	3186	21.02
Ruthenium, Ru	2334	12.37
Osmium, Os	3033	22.61
Rhodium, Rh	1964	12.45
Iridium, Ir	2466	22.65

When developing high-temperature materials systems for structural applications, some key properties such as density, melting point, ductility, creep and oxidation resistance have to be taken into consideration. HEAs can be considered as new types of high-temperature alloys as they possess softening resistance and slow diffusion kinetics at higher temperatures. Refractory high-entropy alloys (RHEAs) based on group IV (Ti, Zr, Hf), V (V, Nb, Ta) and VI (Cr, Mo, W), are particularly attractive for their potential in important high-temperature applications. Until now, RHEAs are not mature and there are not many studies as compared to 3d transition metal containing HEAs. Microstructures of RHEAs usually consist of single bcc phase or bcc plus

Laves phase, considering if Cr or V are also present with other metals. Most of the reported mechanical properties for RHEAs contain only hardness and compression test results, and are rather limited with respect to the tension test data. Some results for as-cast RHEAs are shown in Table 8.

**Table 8: Compression testing results for various as-cast RHEAs.**

Alloy	Phase constitution	$\rho$ ( $\text{g/cm}^3$ )	$\sigma_y$ (MPa)	$\epsilon$ (%)	Reference
Al <sub>0.25</sub> NbTaTiV	bcc	8.80	1330	>50	[69]
Al <sub>0.5</sub> NbTaTiV	bcc	8.46	1012	>50	[69]
AlNbTaTiV	bcc	7.89	991	>50	[69]
CrHfNbTiZr	bcc + laves + laves	8.24	1375	2.8	[70]
HfNbTiVZr	bcc + unknown	8.06	1170	30	[70]
MoNbTaVW	bcc	12.36	1246	1.7	[15]
MoNbTaW	bcc	13.75	1058	2.6	[15]
NbTaTiV	bcc	9.17	1092	>50	[69]

Al<sub>x</sub>NbTaTiV (x= 0.25 to 1) and HfNbTiVZr showed sufficient room temperature compressive ductility indicating that these alloys might possess tensile ductility. However, fracture examination of specimens revealed only cleavage failure, with no signs for ductile fracture. CrHfNbTiZr has a high  $\sigma_y$  but it behaves as a brittle material at room temperature and requires further improvements through microstructural control and compositional variations. Senkov et al. studied MoNbTaVW (Mo<sub>25</sub>Nb<sub>25</sub>Ta<sub>25</sub>V<sub>25</sub>W<sub>25</sub>) and MoNbTaW (Mo<sub>25</sub>Nb<sub>25</sub>Ta<sub>25</sub>W<sub>25</sub>), produced by vacuum arc melting [15]. In the as-cast condition, these alloys consist of a single-phase bcc phase and have a dendritic microstructure. These RHEAs have very high microhardness of Hv = 4.46 GPa and 5.42 GPa, for MoNbTaW and MoNbTaVW respectively. Another prominent feature of

these alloys is that their high yield strength could be maintained over 800 °C, which outperformed some Ni-based superalloys, Haynes 230 [71] and Inconel 718 [72], as shown in Fig. 10 [15].

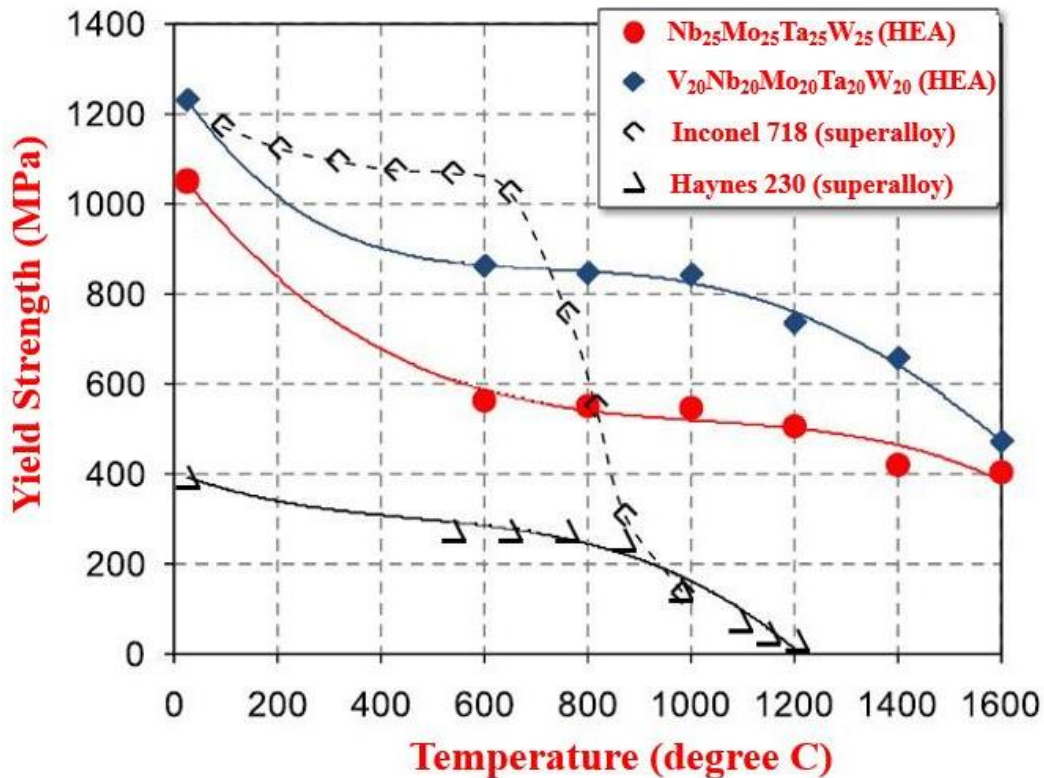


**Figure 10: Yield strength variation with temperature of two different RHEAs MoNbTaW and MoNbTaVW; and the two nickel-base superalloys Haynes 230 and Inconel 718 [15], published and edited with permission from Institute for Scientific Information.**

Yield strength decreased to 405 MPa for the MoNbTaW alloy, and 470 MPa for the MoNbTaVW alloy at the maximum studied temperature which is 1600 °C. Between 600 and 1000 °C, both alloys showed plastic flow with compressive strain above 10-15%. It is believed that the strong resistance to high-temperature softening, in comparison to superalloys, might be due to slow diffusion kinetics among RHEAs and partly because of the high  $T_m$ . Despite very high temperature strength, there is one big concern for RHEAs, i.e., their lack of room

temperature ductility. Both MoNbTaW and MoNbTaVW fractured at a mere elongation of 2.6 % and 1.7 %, respectively, at room temperature under compression loading, which is not acceptable for structural applications. It is important to note here that most of the existing RHEAs lack room-temperature ductility and one of the main challenge to utilize RHEAs as structural materials is therefore their room temperature brittleness. A few RHEAs, which are reported to possess tensile ductility at room temperature include quaternary HfNbTiZr [73], Ta<sub>x</sub>HfZrTi [74] and equiatomic quinary HfNbTaTiZr [33]. Therefore, to further explore the potential of RHEAs, it is important to develop new ductile RHEAs. It is also critical to achieve scientific understanding of the mechanisms controlling ductility, by proposing a guideline to develop ductile RHEAs, while bearing in mind that the corrosion and oxidation resistance of alloys at higher temperatures are also important factors in determining their long term stability. Here we shall focus initially on the alloy design related to the development of RHEAs with optimum *strength and ductility*.

### **3.6 Theories for ductility**

Ductility is the potential of a material to deform plastically prior to fracturing. It is related to both material properties and test conditions, which can include grain size, ease of dislocation generation, dislocation density and their mobility, yield strength, surface energy, as well as temperature and strain rate. Given the large number of variables that influence ductility, it is very difficult to improve the inherent ductility. One way to enhance ductility is to control extrinsic features of the alloy (e.g., through grain size modification and secondary particles/precipitate distribution) [75]. This can help limiting the crack propagation and postpone material failure. Several theories have been proposed in the past which link basic crystal properties to inherent ductility. Rice and Thomson have proposed a ratio  $\mu b/\gamma$  to categorize materials as per their brittle or ductile nature. It consists of  $\mu$ , the shear modulus of the material,  $b$ , the Burgers vector and  $\gamma$ ,

he surface energy. Materials for which the ratio  $\mu b/\gamma$  exceeds  $\sim 10$  would be brittle, while materials with the ratio of  $\mu b/\gamma$  less than  $\sim 7.5$  would likely behave in a ductile manner [76]. Chan analyzed the fracture toughness in a quaternary niobium based alloy system by correlating the number of s+d electrons per atoms to the elastic constants [77]. He utilized the ratio of the surface energy to the Peierls–Nabarro (P-N) barrier energy and the ratio of the surface energy to the unstable stacking fault energy [78, 79]. The tensile ductility and fracture toughness of Nb-Ti-Cr-Al solid solution alloys are improved when the number of (d+s) electrons per atom in the alloy is decreased through alloying, and the contrary is true when the number of (d+s) electrons per atom is increased [77]. It is concluded that the number of (d+s) electrons has an influence on the elastic properties, dislocation mobility and P–N barrier energy. Qi utilized first-principles calculations to study the intrinsic ductility or brittleness of alloys based upon group VI elements such as W and Mo. He proposed that such alloys can become intrinsically ductile if their average valence electron numbers are decreased, which can be controlled by alloying. First-principles calculations show that alloying pure group VI element Mo/W with group IV (Ti, Zr, Hf) or group V transition metals can transform them into intrinsically ductile materials [80].

Most of the reported RHEAs show low to medium high compressive plastic strain at room temperature [11, 15], but engineering and structural applications require significant mechanical properties in loading under tension rather than compression. Therefore, efforts were carried out to design ductile RHEAs, utilizing valence electron concentrations (*VEC*) which has been proven useful in ductilizing simple refractory alloys [80]. *VEC* is also quite useful in controlling the hexagonality of  $\text{Co}_3\text{V}$  alloys related to the room temperature ductility where ordered hexagonal alloys are brittle due to the limited number of slip systems [81]. *VEC* is the sum of electrons

present in the valence band, inclusive of the *d*-electrons [82, 83], obtained by the weighted average of each constituent, shown in Equation 7:

$$VEC = \sum_i^n x_i (VEC)_i \quad \text{Eq. 7}$$

Where  $(VEC)_i$  is the *VEC* for each constituent element. Guo et al. has used *VEC* to outline the phase stability of fcc or bcc solid solutions among HEAs [17, 37]. It is stated that bcc solid solution will be formed at  $VEC < 6.87$  while fcc phases are found to be stable at higher *VEC* ( $\geq 8$ ). However, this knowledge is still insufficient with respect to alloy design for HEAs with optimum mechanical properties, especially for the design of ductile RHEAs. Here in this work, a new ductile RHEA,  $\text{Hf}_{0.5}\text{Nb}_{0.5}\text{Ta}_{0.5}\text{Ti}_{1.5}\text{Zr}$  is proposed using the *VEC* concept. This new RHEA is performing superior than previously developed ductile RHEAs and importantly, the mechanism and direction for ductilizing RHEAs using the electron theory is proposed (paper III).

### 3.7 Thermo-mechanically treated RHEAs

Development of materials with high strength combined with good formability, is always of prime interest in materials science. Thermo-mechanical treatments for microstructure control, such as cold rolling and subsequent annealing are utilized to manipulate materials microstructure and properties, and are critical for structural applications.  $\text{HfNbTaTiZr}$ , a single phase bcc material is one of the very few materials among RHEAs which possess room temperature ductility and have been studied using cold rolling and annealing [84]. Material characterization in the as-cast state revealed microstructure consisting of typical dendritic morphology, which transformed into a coarse equiaxed grain structure when exposed to rolling and annealing. This alloy was subjected to 86.4 % reduction in thickness by cold rolling prior to annealing at varying temperatures. Annealing at 1000 °C resulted in tensile stress and elongation to fracture of around 1.2 GPa and

9.7 % respectively. The material retained single-phase bcc structure. However, the role of plastic deformation and annealing on the microstructure of RHEAs has been studied to a very limited extent [84]. To explore their potential, in this study,  $\text{Hf}_{0.5}\text{Nb}_{0.5}\text{Ta}_{0.5}\text{Ti}_{1.5}\text{Zr}$ , performing better than previously developed ductile RHEAs (paper III), was also subjected to approx. 87 % thickness reduction via cold rolling and later annealed at three different conditions i.e. a) Sample A (1200 °C for 1 min), b) Sample B (1250 °C for 2 min), and c) Sample C (1250 °C for 5 min). Our goal here was to perform a study on the mechanical properties on the  $\text{Hf}_{0.5}\text{Nb}_{0.5}\text{Ta}_{0.5}\text{Ti}_{1.5}\text{Zr}$  RHEA through microstructure refinement, especially to control grain size for further improvement in the mechanical properties of single phase alloys [85].

### **3.8 Oxidation resistance of RHEAs with optimum mechanical properties**

Despite numerous efforts, the use of refractory alloys in high-temperature applications is still limited mainly due to their poor oxidation resistance, which becomes worse with increasing temperature [86]. Group IV elements Ti, Zr, and Hf have the highest thermodynamic activity towards oxygen, and group V elements such as Nb and Ta are also subject to strong oxidation at temperatures above 400 °C [67]. In the past, plenty of work has been done to enhance the oxidation resistance of refractory alloys through alloying additions which include elements such as Al, Cr and Si. These elements can enable the formation of protective oxide layers, i.e.,  $\text{Al}_2\text{O}_3$ ,  $\text{Cr}_2\text{O}_3$  and  $\text{SiO}_2$ , if present in sufficient amounts [87, 88]. The addition of oxide forming elements comes with a compromise though, since Al, Cr and Si are chemically active and have very negative heats of formation with other metallic elements. They therefore tend to promote the formation of brittle intermetallic compounds such as  $\text{Nb}_3\text{Al}$ ,  $\text{NbCr}_2$ ,  $\text{Nb}_5\text{Si}_3$ , and  $\text{MoSi}_2$ , leading to the poor room temperature ductility/toughness [89]. The development of refractory alloys with enhanced oxidation resistance and optimal mechanical properties, has been a formidable

challenge [90]. The concept RHEAs, is believed to hold the promise in this regard. Nevertheless, there is still a long way to go before RHEAs can be really used for high-temperature applications. Based on the known facts for refractory alloys, the oxidation resistance could also be problematic for RHEAs, but there exists only limited work towards the study of high-temperature oxidation of RHEAs [91, 92]. To name a few examples,  $\text{CrMo}_{0.5}\text{NbTa}_{0.5}\text{TiZr}$  was reported to form a protective oxide scale at 1000 °C after 100h of exposure, but the material lacked room-temperature ductility because of the presence of brittle Laves phase [16, 92];  $\text{AlCrMoTaTi}$  RHEAs seemed to form a protective and dense alumina scale below the rutile layer after air exposure at 1000 °C for 48h, with a low mass gain and its oxidation kinetics adhering to the parabolic rate law, but there is no report on its mechanical properties [93]. The  $\text{AlCrMoNbTi}$  system, upon alloying with Si, showed some improved oxidation behavior, but its mechanical properties were poor and it showed no evidence of plastic deformation at room temperature [94, 95]. Up to now, there is a lack of clear information on the oxidation resistance for ductile RHEAs. Here during the course of this work, the oxidation behavior of a previously developed ductile RHEA with a single-phase bcc structure is studied.

### **3.9 Accelerated oxidation and alloying**

It is widely reported that group IV (Ti, Zr, Hf) elements dissolve large amount of oxygen, which can be either present in the form of metal oxides or interstitially dissolved oxygen atoms. The solubility of oxides decreases towards group V (V, Nb, Ta) and VI (Cr, Mo, W) elements. Some of the most thermodynamically stable oxides with the lowest standard free energy of formation are formed by group IV elements such as  $\text{TiO}_2$  and  $\text{ZrO}_2$  [96]. These oxides can lead to internal oxidation followed by formation of other complex oxide structures. For some conventional refractory intermetallics such as  $\text{NbAl}$ ,  $\text{NbAl}_3$ , and  $\text{MoSi}_2$ , oxidation becomes very severe and

leads to total disintegration of the material into powder, referred to as pesting or pest disintegration [97, 98]. The mechanism and temperature range for pesting vary for different intermetallic alloys. Pesting of  $\text{MoSi}_2$  by oxidation in air, has been observed at temperatures between 375 and 500 °C [99, 100]. In contrast,  $\text{MoSi}_2$  oxidized at 550 °C exhibits severe cracking but no pesting, while  $\text{MoSi}_2$  oxidized at 350 °C or at and above 600 °C remains intact. Pesting of  $\text{MoSi}_2$  produces powdery products consisting of  $\text{MoO}_3$  whiskers,  $\text{SiO}_2$  clusters, and residual  $\text{MoSi}_2$  crystals. In the literature, the mechanism for pesting in  $\text{MoSi}_2$  is not unified. According to Chou and Nieh [101], the morphologies of the disintegrated powders indicate that the pesting of  $\text{MoSi}_2$  involves two major kinetic processes, i.e., volume diffusion and grain boundary diffusion of oxygen. For the pesting of single-crystal  $\text{MoSi}_2$ , the volume diffusion is the dominating process and it results initially in the formation of a transient Si-Mo-O oxide, which subsequently converts into loosely packed  $\text{MoO}_3$  and  $\text{SiO}_2$ , leading to surface recession. In poly-crystal  $\text{MoSi}_2$ , the grain boundary diffusion process also takes place, which is a more rapid kinetic process and causes the formation of  $\text{MoO}_3$  and  $\text{SiO}_2$  at grain boundaries. The formation of  $\text{MoO}_3$  and  $\text{SiO}_2$  at grain boundaries not only results in a large local volume change, but also produces internal pressures because  $\text{MoO}_3$  is volatile. Both of these two factors generate local stresses at grain boundaries and give rise to intergranular decohesion as well as microcrack formation, and eventually lead to the disintegration of  $\text{MoSi}_2$ . The concurrent reproduction of internal interfaces and cracks during pesting makes the total disintegration of  $\text{MoSi}_2$  occur in a catastrophic manner. McKamey et al. had a different opinion and they basically thought the pesting in  $\text{MoSi}_2$  is the result of oxidation in pre-existing cracks and pores [99], They reckoned that since the oxygen solubility in  $\text{MoSi}_2$  is negligible, internal oxidation and intergranular oxidation are not supposed to happen. Instead, they thought the pesting proceeds by the following steps: (i) oxygen initially moves into the specimen via pre-existing pores and/or cracks; (ii)  $\text{MoO}_3$  along with some  $\text{SiO}_2$

form on crack walls; (iii) the stresses produced by the volume expansion during transformation from  $\text{MoSi}_2$  to  $\text{MoO}_3$  push the material apart; (iv) after easy paths like pre-existing cracks and pores are exhausted, oxidation continues along other paths to produce finer disintegrated powder. The mechanism that was proposed by McKamey et al. is favored by us, considering the fact that the solubility of oxygen is negligible in  $\text{MoSi}_2$  [100]. Pesting of  $\text{NbAl}_3$  occurs between 550 and 950 °C, with a maximum between 650 and 850 °C [98, 100]. The pesting of  $\text{NbAl}_3$  is believed to occur via these steps: (i) selective oxidation of Al with  $\text{Al}_2\text{O}_3$  scale formation, preferentially along grain boundaries underneath the outer scale, results in Al depletion of the  $\text{NbAl}_3$  phase; (ii) the Al depletion leads to a phase transformation from  $\text{NbAl}_3$  to  $\text{Nb}_2\text{Al}$  at the grain boundaries, which causes fissure formation at the grain boundaries and cracking of the outer scale; (iii) oxygen from the atmosphere penetrates into the fissures and  $\text{Al}_2\text{O}_3$  is formed on the surfaces of the separated grains within the material; (iv) new regions of  $\text{Nb}_2\text{Al}$  grow and new holes form deep inside the materials, and oxidation goes on repeatedly, resulting in the complete disintegration [100]. During the high temperature oxidation studies of  $\text{Hf}_{0.5}\text{Nb}_{0.5}\text{Ta}_{0.5}\text{Ti}_{1.5}\text{Zr}$ , pesting was observed. Therefore the pesting phenomenon and its mechanism for RHEAs is studied which will provide important input to the further development of RHEAs as novel high-temperature materials (paper IV). As mentioned above, since pesting is believed to be connected to the mismatch in volume expansion between the base RHEA and the formed complex oxide, efforts were made trying to reduce such a mismatch. It was found that by removing both Hf and Zr at the same time, two elements with larger atomic radii than other elements, from  $\text{Hf}_{0.5}\text{Nb}_{0.5}\text{Ta}_{0.5}\text{Ti}_{1.5}\text{Zr}$ , the pesting can be avoided in the ternary  $\text{Nb}_{0.5}\text{Ta}_{0.5}\text{Ti}_{1.5}$  alloy. To further improve the oxidation resistance, more than just avoiding the pesting,  $\text{Nb}_{0.5}\text{Ta}_{0.5}\text{Ti}_{1.5}$  was alloyed with 28.6 at.% Al to form  $\text{AlNb}_{0.5}\text{Ta}_{0.5}\text{Ti}_{1.5}$ .  $\text{AlNb}_{0.5}\text{Ta}_{0.5}\text{Ti}_{1.5}$  did not pest in the pesting temperature window for  $\text{Hf}_{0.5}\text{Nb}_{0.5}\text{Ta}_{0.5}\text{Ti}_{1.5}\text{Zr}$ , but was brittle in the as-cast state, showing no any

indication of plastic deformation. To reduce brittleness, the Al content in  $\text{AlNb}_{0.5}\text{Ta}_{0.5}\text{Ti}_{1.5}$  was reduced to 16.7 at.%, forming  $\text{Al}_{0.5}\text{Nb}_{0.5}\text{Ta}_{0.5}\text{Ti}_{1.5}$ . Again,  $\text{Al}_{0.5}\text{Nb}_{0.5}\text{Ta}_{0.5}\text{Ti}_{1.5}$  alloy did not experience pesting, but the room-temperature brittleness was still an issue. Therefore, the Al content was further reduced to 15.4 at.%, and some amount of Cr was added to compensate for the reduced Al content, a sufficient amount of which is needed for the oxidation resistance, considering that Nb, Ta and Ti have poor oxidation resistance at high temperatures [88]. As such, a new alloy  $\text{Al}_{0.5}\text{Cr}_{0.25}\text{Nb}_{0.5}\text{Ta}_{0.5}\text{Ti}_{1.5}$  was formulated. It is important to remind here that designing the amount of alloying additions on Al and Cr has to consider both the improved oxidation resistance and the maintenance of tensile ductility.  $\text{Al}_{0.5}\text{Cr}_{0.25}\text{Nb}_{0.5}\text{Ta}_{0.5}\text{Ti}_{1.5}$  showed a clear sign for ductility, as the as-cast specimen could be easily bent 90 degrees without any breakage. However, the initial oxidation studies showed that although  $\text{Al}_{0.5}\text{Cr}_{0.25}\text{Nb}_{0.5}\text{Ta}_{0.5}\text{Ti}_{1.5}$  did not pest in a wide temperature range from 600 to 1200 °C, it was embrittled very possibly due to internal oxidation. Therefore, the oxidation resistance of  $\text{Al}_{0.5}\text{Cr}_{0.25}\text{Nb}_{0.5}\text{Ta}_{0.5}\text{Ti}_{1.5}$  needs to be further improved. One possible strategy is to slightly increase the Al and/or Cr content, but their amounts need to be carefully adjusted, since excessive Cr can promote the formation of brittle Laves phase, while Al tends to form strong bonds with other constituent refractory elements, also leading to brittleness [88].

### **3.10 Aluminizing**

Another strategy to improve high temperature oxidation resistance is to carry out surface modification by the coating treatment that can enrich the surface of a base RHEA with oxide forming protective elements such as Al, Cr or Si. In this regard, one particular method known as the pack cementation aluminizing process, promotes formation of aluminum-rich coatings to enhance the oxidation resistance and appears to be a very useful technique [102]. Aluminizing

has been reportedly utilized on the Ni based superalloys blades in the turbine engines, titanium base alloys and niobium base alloys for protection against oxidation [103-109]. Among Ni based super-alloys, aluminum rich coatings in the form of NiAl cover layer, can protect the surface of turbine blades against oxidation [103]. Ti<sub>3</sub>Al-based alloys have good high-temperature strength, but their poor oxidation resistance above 650 °C limits their applications. After aluminizing, oxidation resistance has been reportedly improved till 1100 °C [107]. Similarly, high-temperature working limit of niobium aluminide-based alloys can be enhanced to 850 °C by aluminide-based diffusion coatings [108]. Aluminizing is carried out in a dry atmosphere and consists of four major constituents: a) the metal substrate which needs to be aluminized; b) the masteralloy (elemental or alloyed powder which will be deposited on the substrate and usually comprises of Ni and/or Al, Al and/or Cr, Cr and/or Si; c) halide salt activator (NH<sub>4</sub>Cl, NaF, NaCl etc.); and d) inert filler powder (Al<sub>2</sub>O<sub>3</sub>, SiO<sub>2</sub> or SiC) [102]. There is a reported role of pack composition chemistry and coating conditions, which can lead to optimum oxidation resistant coatings upon oxygen exposure at high temperatures. During pack-cementation, Al concentration in the depositing material defines the activity of the Al vapor towards the substrate, and are generally classified to high Al activity pack and low Al activity pack, where the prior results in an increased Al activity inwards, while the later increases the substrate metal diffusion outwards. In general, the use of unalloyed aluminum in the coating medium is referred to as high Al activity pack, and if the aluminum is alloyed, the coating process is defined as a low Al activity pack [109]. Based upon the Al activity, the coating structure of aluminized Ni based alloy can be controlled. Higher Al activity results in Ni<sub>2</sub>Al<sub>3</sub> which is not favorable, while low Al activity can lead to the beta NiAl phase, which is preferable and has superior oxidation and mechanical properties [110]. Inert filler is useful in controlling the deposition activity and prevents direct contact of substrate with Al droplets at the coating temperature. Aluminizing temperature affects

the rate and efficiency of deposition, overall mechanical and physical properties of the material and the final performance of the substrate. Another parameter is aluminizing time, which is related to the coating thickness through the parabolic growth equation [111]. Generally, thinner coatings have lower internal stresses from the CTE mismatch and hence, lead to lesser cracks within the aluminized layer, indicating that cracking within the aluminized layer can be avoided by controlling the aluminizing time. All of these factors indicate that the choice of aluminizing pack compositions and conditions is critical and can vary for each particular alloy. Aluminizing conditions suitable for Ni based super alloys may not always apply for Co-based super alloys [110]. Aluminizing employs simple equipments and can result in cost effective and homogeneous coatings, which can enable to improve the high temperature oxidation resistance. Aluminizing is carried out through the pack cementation process in an alumina crucible, with a typical schematic shown in Fig. 11.

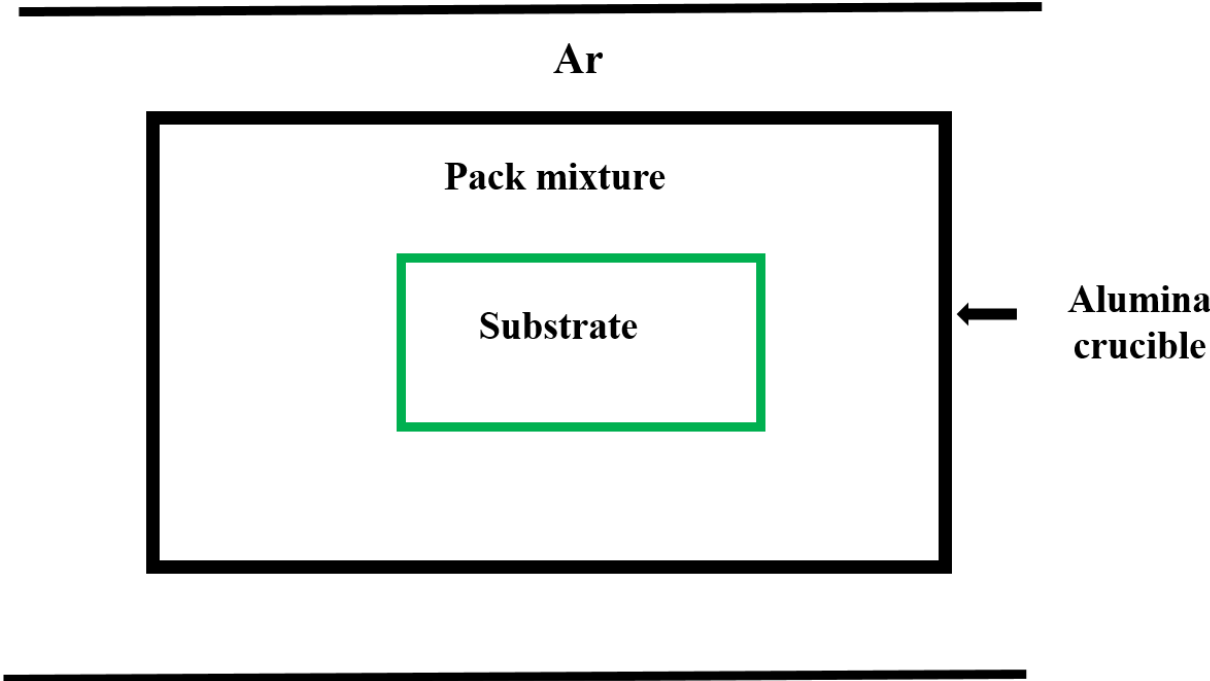


**Figure 11: Schematic for aluminizing (pack-cementation) process.**

Aluminized coatings can help to form protective and continuous  $\text{Al}_2\text{O}_3$  layer upon exposure to air at high temperatures. In fact, it is not only restricted to formation of Al-rich layers but also extended to Cr and Si-rich layers [107]. Among some of the studies, TiAl being one of the potential candidates for high temperature systems, is reported by Zhou et al. to improve the oxidation resistance at temperatures above  $800\text{ }^\circ\text{C}$  [112]. Aluminizing was carried with halide-activated pack cementation mixture of 15 wt.% Al, 82 wt.%  $\text{Al}_2\text{O}_3$  and 3 wt.%  $\text{NH}_4\text{Cl}$ , resulting in the formation of stable  $\text{TiAl}_3$  layer on the TiAl substrate, thus improving the cyclic oxidation resistance. In another study by Koo et al. to improve oxidation resistance of  $\text{Ti}_3\text{Al-Nb}$  alloys, pack cementation of Al, Cr and Si coatings were carried out. It was reported that Al rich (aluminized coating with a single layer of the  $\text{TiAl}_3$  phase), Cr rich (chromized coating comprising of a Cr-rich beta phase) and Si rich (siliconized coating of multilayer structure with the composition of  $\text{TiAl}_2$ , TiAl,  $\text{TiSi}_2$  and TiSi) coatings were formed. It was found that oxidation resistance of Al and Si coatings at elevated temperature up to  $1100\text{ }^\circ\text{C}$  is superior as compared to chromized coatings [107]. Within HEAs, there is only one study regarding aluminizing, and was carried out on  $\text{Al}_{0.2}\text{Co}_{1.5}\text{CrFeNi}_{1.5}\text{Ti}_{0.3}$  HEA to improve the oxidation resistance. After aluminizing, the oxidation resistance of HEA improved significantly, up to  $1273\text{ K}$  for 441h [113]. Here in this work, two ductile RHEAs,  $\text{Hf}_{0.5}\text{Nb}_{0.5}\text{Ta}_{0.5}\text{Ti}_{1.5}\text{Zr}$  that is subject to pesting and  $\text{Al}_{0.5}\text{Cr}_{0.25}\text{Nb}_{0.5}\text{Ta}_{0.5}\text{Ti}_{1.5}$  that is subject to embrittlement upon oxidation, are aluminized using varying master alloys and aluminizing time, aiming to identify optimal aluminizing conditions for enhancing the oxidation resistance in both cases (paper V).

**Table 9: Aluminizing conditions for Hf<sub>0.5</sub>Nb<sub>0.5</sub>Ta<sub>0.5</sub>Ti<sub>1.5</sub>Zr (S1).**

<b>Sample reference</b>	<b>Pack composition</b>	<b>Aluminizing time</b>	<b>Oxidation condition</b>
S1-NiAl60-5h-A	49.0 wt.% Ni <sub>40</sub> Al <sub>60</sub> (at.%) + 49.0 wt.% Al <sub>2</sub> O <sub>3</sub> + 2.0% wt.% NH <sub>4</sub> Cl	5h	as-aluminized
S1-NiAl60-5h-O	49.0 wt.% Ni <sub>40</sub> Al <sub>60</sub> (at.%) + 49.0 wt.% Al <sub>2</sub> O <sub>3</sub> + 2.0% wt.% NH <sub>4</sub> Cl	5h	800 °C/5h
S1-NiAl54-5h-A	49.0 wt.% Ni <sub>46</sub> Al <sub>54</sub> (at.%) + 49.0 wt.% Al <sub>2</sub> O <sub>3</sub> + 2.0% wt.% NH <sub>4</sub> Cl	5h	as-aluminized
S1-NiAl54-5h-O	49.0 wt.% Ni <sub>46</sub> Al <sub>54</sub> (at.%) + 49.0 wt.% Al <sub>2</sub> O <sub>3</sub> + 2.0% wt.% NH <sub>4</sub> Cl	5h	800 °C/5h
S1-Al, Cr-5h-A	24.5 wt.% Al + 24.5 wt.% Cr + 49.0 wt.% Al <sub>2</sub> O <sub>3</sub> + 2.0% wt.% NH <sub>4</sub> Cl	5h	as-aluminized
S1-Al, Cr-5h-O	24.5 wt.% Al + 24.5 wt.% Cr + 49.0 wt.% Al <sub>2</sub> O <sub>3</sub> + 2.0% wt.% NH <sub>4</sub> Cl	5h	800 °C/5h
S1-NiAl60-2h-A	49.0 wt.% Ni <sub>40</sub> Al <sub>60</sub> (at.%) + 49.0 wt.% Al <sub>2</sub> O <sub>3</sub> + 2.0% wt.% NH <sub>4</sub> Cl	2h	as-aluminized
S1-NiAl60-2h-O	49.0 wt.% Ni <sub>40</sub> Al <sub>60</sub> (at.%) + 49.0 wt.% Al <sub>2</sub> O <sub>3</sub> + 2.0% wt.% NH <sub>4</sub> Cl	2h	800 °C/5h
S1-Al, Cr-2h-A	24.5 wt.% Al + 24.5 wt.% Cr + 49.0 wt.% Al <sub>2</sub> O <sub>3</sub> + 2.0% wt.% NH <sub>4</sub> Cl	2h	as-aluminized
S1-Al, Cr-2h-O	24.5 wt.% Al + 24.5 wt.% Cr + 49.0 wt.% Al <sub>2</sub> O <sub>3</sub> + 2.0% wt.% NH <sub>4</sub> Cl	2h	800 °C/5h

**Table 10: Aluminizing conditions for Al<sub>0.5</sub>Cr<sub>0.25</sub>Nb<sub>0.5</sub>Ta<sub>0.5</sub>Ti<sub>1.5</sub> (S2)**

<b>Sample reference</b>	<b>Pack composition</b>	<b>Aluminizing time</b>	<b>Oxidation condition</b>
S2-NiAl54-5h-A	49.0 wt.% Ni <sub>46</sub> Al <sub>54</sub> (at.%) + 49.0 wt.% Al <sub>2</sub> O <sub>3</sub> + 2.0% wt.% NH <sub>4</sub> Cl	5h	as-aluminized
S2-NiAl54-5h-O	49.0 wt.% Ni <sub>46</sub> Al <sub>54</sub> (at.%) + 49.0 wt.% Al <sub>2</sub> O <sub>3</sub> + 2.0% wt.% NH <sub>4</sub> Cl	5h	800 °C/5h
S2-NiAl60-2h-A	49.0 wt.% Ni <sub>40</sub> Al <sub>60</sub> (at.%) + 49.0 wt.% Al <sub>2</sub> O <sub>3</sub> + 2.0% wt.% NH <sub>4</sub> Cl	2h	as-aluminized
S2-NiAl60-2h-O	49.0 wt.% Ni <sub>40</sub> Al <sub>60</sub> (at.%) + 49.0 wt.% Al <sub>2</sub> O <sub>3</sub> + 2.0% wt.% NH <sub>4</sub> Cl	2h	800 °C/5h
S2-Al, Cr-2h-A	24.5 wt.% Al + 24.5 wt.% Cr + 49.0 wt.% Al <sub>2</sub> O <sub>3</sub> + 2.0% wt.% NH <sub>4</sub> Cl	2h	as-aluminized
S2-Al, Cr-2h-O	24.5 wt.% Al + 24.5 wt.% Cr + 49.0 wt.% Al <sub>2</sub> O <sub>3</sub> + 2.0% wt.% NH <sub>4</sub> Cl	2h	800 °C/5h

## **4 Experimental methods**

### **4.1 Arc melting**

HEAs were prepared in an arc-melting equipment supplied by Edmund Bühler Company. Melting was carried out through vacuum arc-melting a mixture of constituent elements with purity greater than 99.9 wt. % in a Ti-gettered high-purity argon atmosphere. The melting and flipping of samples was repeated at least five times to achieve a good chemical homogeneity of the alloy. Arc-melting furnace utilizes a non-consumable tungsten electrode to generate electric arc that heats up the gas and creates plasma. High vacuum is obtained using both a rotary and a diffusion pump which can achieve a vacuum of  $10^{-5}$  mbar. The casting mold and melting plate on which the raw material was placed, are made out of copper in order to conduct heat quickly. The heating chamber and the crucible plate are also water-cooled by an external chiller in order to avoid overheating during the melting process.

### **4.2 Vickers hardness measurements**

Vickers hardness measurement is an indentation technique in which the diamond indenter with the geometry of a pyramid is forced onto the surface of a mechanically grinded and polished sample. The diagonals of the indent are measured and Vickers hardness are determined using Equation 8, where P is load (N) and d (mm) is the mean length of diagonals. For hardness measurements in the present study, a load of 9.8 N (1kg) is applied for 15 s.

$$HV=0.01819 P/d^2 \quad \text{Eq. 8}$$

### **4.3 X-ray diffraction**

X-ray diffraction is used for phase identification in materials. The atoms or molecules of the crystal cause X-rays to diffract into certain directions, producing secondary waves spreading from

electrons. Such waves cancel each other in most directions through destructive interference and constructively in some directions, determined by Bragg's law given in Equation 9, where  $n$  is the diffraction order,  $\lambda$  is the wavelength of the X-ray source,  $d$  is the interplanar distance and  $\Theta$  is the diffraction angle [114].

$$n\lambda = 2d\sin\Theta \quad \text{Eq. 9}$$

Diffraction planes are then matched to those of standard databases. In this work, a Bruker AXS D8 X-ray diffractometer (XRD) is used equipped using Cr- $K_{\alpha}$  radiation. The generator was set at 35 kV acceleration voltage and 40 mA current. The phase constitution of oxidation products was characterized by XRD, MiniFlex 600, Rigaku using Cu- $K_{\alpha}$  radiation (paper IV and V).

#### **4.4 Oxidation studies**

Oxidation tests were carried out in a horizontal tube furnace that is opened on both ends, and has a maximum working temperature of around 1400 °C. During the oxidation tests, specimens were positioned in the heating zone using alumina boats, and taken out immediately from the furnace to cool in air when the supposed oxidation tests were completed. The oxidation of alloys was monitored by the weight change per unit area as a function of time, and by visual observation.

#### **4.5 Microstructural investigation**

Prior to studying the microstructure by use of microscopy, the material was mounted with polyfast by hot mounting method, using the CitoPress 20 equipment. Samples were then prepared by grinding with SiC papers, followed by fine polishing using cloth and diamond-paste suspension of 3 and 1  $\mu\text{m}$ . Both an optical microscope and a scanning electron microscope (SEM) were used to evaluate microstructure and fractured tensile specimens. Stereomicroscope was used for investigations at lower magnification. For stereomicroscopic imaging, a Zeiss discovery V20

machine was used together with AxioVision image analysis software. In comparison, SEM makes use of a focused electron beam for imaging. Electrons are generated either via field emission gun or by means of a source utilizing tungsten or LaB<sub>6</sub>. Generated electrons are accelerated through apertures at a rather high potential (keV). The beam is then focused by means of various electromagnetic lenses; and scanning coils are used to move the electron beam over the sample surface [115]. Incoming electrons interact with the sample, and electrons emitted from the sample surface are detected as a signal, later amplified and displayed on a TV-screen. SEM has advantages over optical microscopy in a way that depth of field is much superior, and the spatial resolution is also much better. By choosing an appropriate detector such as a backscattered electron detector, one can perform imaging using atomic number contrast. The microstructure of HEA samples were studied on polished and electrochemically etched specimen using a LEO Gemini 1550 SEM equipped with energy dispersive spectrometer [116] and Oxford Nordlys electron backscatter diffraction (EBSD) detector. EDS, which employs X-ray signal for chemical compositional identification, was performed using Aztec software. The EBSD technique was used for RHAEs during the course of this work, as it is a useful technique for obtaining microstructural and crystallographic information. Upon interaction with crystalline sample, the electron beam generates diffraction pattern which can be detected by a fluorescent screen and a CCD camera. The diffraction patterns are referred to as Kikuchi lines, which allow to identify the material's structure, grain orientation/size and texture etc. [117]. The acceleration voltage of the electron beam was set at 20 kV and a step size of 1.3 μm was used. Phase identification was carried out using Aztec, but the evaluation was performed by HKL Channel 5 software (Oxford Instruments) and inorganic crystal structure database (ICSD) using space group Im-3m with lattice parameters ( $a = 3.38 \text{ \AA}$ ,  $b = 3.38 \text{ \AA}$  and  $c = 3.38 \text{ \AA}$ ). The etchant used to reveal the

microstructure was a mixture of 1.5 ml nitric acid, 5 ml hydrofluoric acid and 45 ml water which was applied for approximately 10 seconds (paper IV).

#### **4.6 Tensile testing**

Rectangular dog-bone-shaped tensile specimen with a gauge length of 12.5 mm, width of 3.2 mm and thickness of 2 mm, were machined from the as-cast ingot by water jet cutting and were tested at room temperature. Tensile testing was carried out using an Instron 5500R electro-mechanic tensile tester, with a strain rate of  $10^{-3} \text{ s}^{-1}$  and tests were carried out according instructions from ASTM standard E8 [118].

#### **4.7 Aluminizing**

Specimens with dimensions of  $5\text{mm} \times 10\text{ mm} \times 10\text{ mm}$  were then cut from the ingots to carry out aluminizing by placing the specimens within a powder mixture as mentioned in Tables 9 and 10, placed in an alumina crucible in a heat-resistant container. This container was placed in a vacuum furnace that was connected to a mechanical rotary pump and evacuated down to  $10^{-1} \text{ Pa}$  at room temperature. After furnace evacuation, Ar was introduced until the pressure reached  $10^5 \text{ Pa}$ , followed by the re-evacuation and flushing with Ar for at least three times. Three different powder mixtures were utilized as pack components with two varying aluminizing times. The furnace was then heated up to  $900 \text{ }^\circ\text{C}$  at a rate of  $10 \text{ }^\circ\text{C}/\text{min}$  and kept at this temperature for 5h and 2h for each selected specimens to complete aluminizing, followed by cooling inside the furnace to room temperature. Specimens after aluminizing were oxidized in air in a box furnace at  $800 \text{ }^\circ\text{C}$  for 5h, the oxidation condition where the most pesting occurs for  $\text{Hf}_{0.5}\text{Nb}_{0.5}\text{Ta}_{0.5}\text{Ti}_{1.5}\text{Zr}$ . Oxidation tests were carried out in a box furnace that can achieve the maximum temperature of around  $1600 \text{ }^\circ\text{C}$ . During the oxidation tests, aluminized specimens were placed in alumina crucibles and positioned in the heating zone when the temperature was stabilized at  $800 \text{ }^\circ\text{C}$ , and

once the supposed oxidation tests were completed, specimens were taken out of immediately from the furnace and cooled in air.



## 5 Summary of Results

### 5.1 The $Md$ concept and HEAs

Initially, we used a single parameter, the average energy of d-orbital levels,  $Md$ , to predict the solid solubility, and more specifically the phase boundaries between fcc/bcc solid solution and topological/geometrical closely packed (TCP/GCP) phases in HEAs (paper I). The  $Md$  parameter can work nicely to predict the solid solubility in fcc structured HEAs containing only 3d transition metals and also the solid solubility in bcc structured HEAs. However, the  $Md$  parameter does not work well for fcc structured HEAs when 4d transition metals are alloyed, and the reason was attributed to the large bond strength of 4d elements. For fcc structured HEAs containing only 3d transition metals, a critical  $Md$  of 0.97 was identified below which the fcc solid solution forms, and beyond which TCP/GCP phases start to form. When 4d transition metals are alloyed, it was found that TCP/GCP phases can form at  $Md$  lower than 0.97, such that there exists no critical  $Md$  to predict the solid solubility limit. By re-inspecting the data point leading to the above conclusion (Fig. 3 in paper I), it is found that TCP/GCP phases already formed in the supposedly fcc solid solution. In other words, TCP/GCP phases form at lower  $Md$  than 0.97, but it could possibly only indicate the critical  $Md$  is lower than 0.97, when 4d transition metals are alloyed. With this thinking in mind, the phase constitutions and corresponding  $Md$  for CoCrFeNi and CoCrFeNiM<sub>x</sub> (M=Zr, Nb, Mo, Ti, Mn, Cu) HEAs are listed in Table 11.

**Table 11: Phase constitutions and d-orbital energy level,  $Md$ , in CoCrFeNiM<sub>x</sub> (M=Mo, Nb, Zr) HEAs. To reveal the phase boundary, phase constitutions and  $Md$  for CoCrFeNi and CoCrFeNiM<sub>x</sub> (M=Ti, Mn, Cu) are also listed.**

Alloy system	Phase	$Md$	Reference
CoCrFeNi	fcc	0.874	[25]
CoCrFeNiCu <sub>0.5</sub> (3d)	fcc	0.845	[47]
CoCrFeNiCu (3d)	fcc	0.822	[32]
CoCrFeNiMn (3d)	fcc	0.890	[8]
CoCrFeNiMo <sub>0.1</sub> (4d)	fcc	0.890	[49]
CoCrFeNiTi <sub>0.3</sub> (3d)	fcc+ $\sigma$ +R	0.971	[51]
CoCrFeNiTi <sub>0.5</sub> (3d)	fcc+ $\sigma$ +Laves+R	1.029	[51]
CoCrFeNiMo <sub>0.3</sub> (4d)	fcc+ $\sigma$	0.921	[50]
CoCrFeNiMo <sub>0.5</sub> (4d)	fcc+ $\sigma$	0.949	[50]
CoCrFeNiMo <sub>0.85</sub> (4d)	fcc+ $\sigma$ + $\mu$	0.992	[50]
CoCrFeNiNb <sub>0.103</sub> (4d)	fcc+Laves	0.905	[119]
CoCrFeNiNb <sub>0.155</sub> (4d)	fcc+Laves	0.920	[119]
CoCrFeNiNb <sub>0.206</sub> (4d)	fcc+Laves	0.934	[119]
CoCrFeNiNb <sub>0.309</sub> (4d)	fcc+Laves	0.963	[119]
CoCrFeNiNb <sub>0.412</sub> (4d)	fcc+Laves	0.990	[119]
CoCrFeNiZr <sub>0.05</sub> (4d)	fcc+Ni <sub>7</sub> Zr <sub>2</sub>	0.899	this work
CoCrFeNiZr <sub>0.1</sub> (4d)	fcc+Ni <sub>7</sub> Zr <sub>2</sub>	0.924	this work
CoCrFeNiZr <sub>0.15</sub> (4d)	fcc+Ni <sub>7</sub> Zr <sub>2</sub> +Laves	0.948	this work
CoCrFeNiZr <sub>0.2</sub> (4d)	fcc+Ni <sub>7</sub> Zr <sub>2</sub> +Laves	0.972	this work
CoCrFeNiZr <sub>0.25</sub> (4d)	fcc+Ni <sub>7</sub> Zr <sub>2</sub> +Laves	0.995	this work
CoCrFeNiZr <sub>0.3</sub> (4d)	fcc+Ni <sub>7</sub> Zr <sub>2</sub> +Laves	1.018	this work
CoCrFeNiZr <sub>0.35</sub> (4d)	fcc+Ni <sub>7</sub> Zr <sub>2</sub> +Laves	1.040	this work
CoCrFeNiZr <sub>0.4</sub> (4d)	fcc+Ni <sub>7</sub> Zr <sub>2</sub> +Laves	1.062	this work
CoCrFeNiZr <sub>0.45</sub> (4d)	fcc+Laves	1.083	this work
CoCrFeNiZr <sub>0.5</sub> (4d)	fcc+Laves	1.104	this work

$Md$  values calculated in Table 11 are also plotted in Fig. 12. Apart from 4d transition metals Zr, Nb, and Mo, 3d transition metals Ti, Mn and Cu are also included, to reveal the phase boundary between the fcc solid solution and intermetallic compounds, including the TCP phase and the  $Ni_7Zr_2$  phase. As seen from Fig. 12, there seems to exist a critical  $Md$  of  $\sim 0.89$  that delineates the phase boundary between the fcc solid solution and intermetallic compounds.

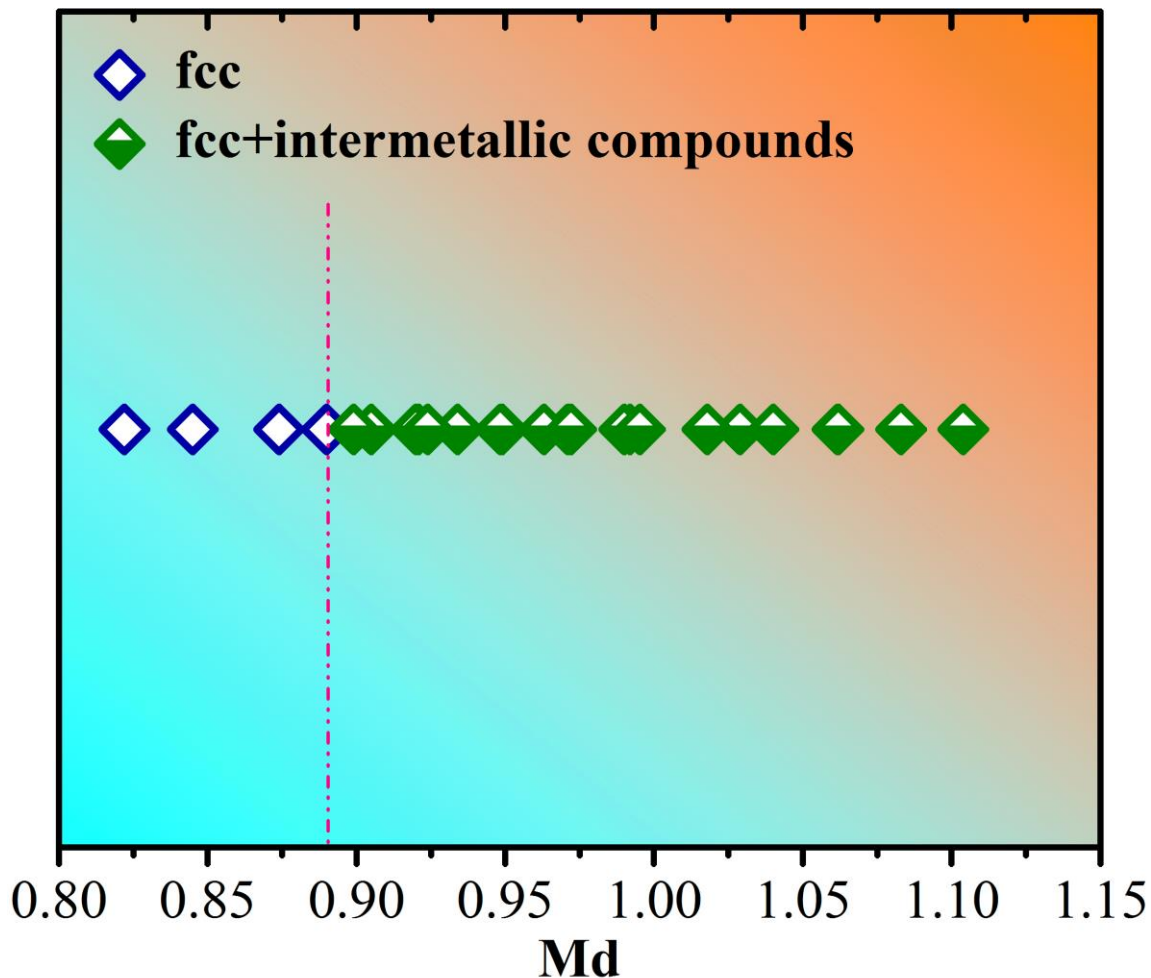


**Figure 12: The parameter  $Md$  and the phase constitution in CoCrFeNi and CoCrFeNiM<sub>x</sub> (M=Zr, Nb, Mo; Ti, Mn, Cu) alloys, published with permission from AIP.**

XRD was also carried out to further confirm the  $Md$  concept by extending it to as-cast CoCrFeNiZr<sub>x</sub> alloys that were prepared in this work as shown in Fig. 13.

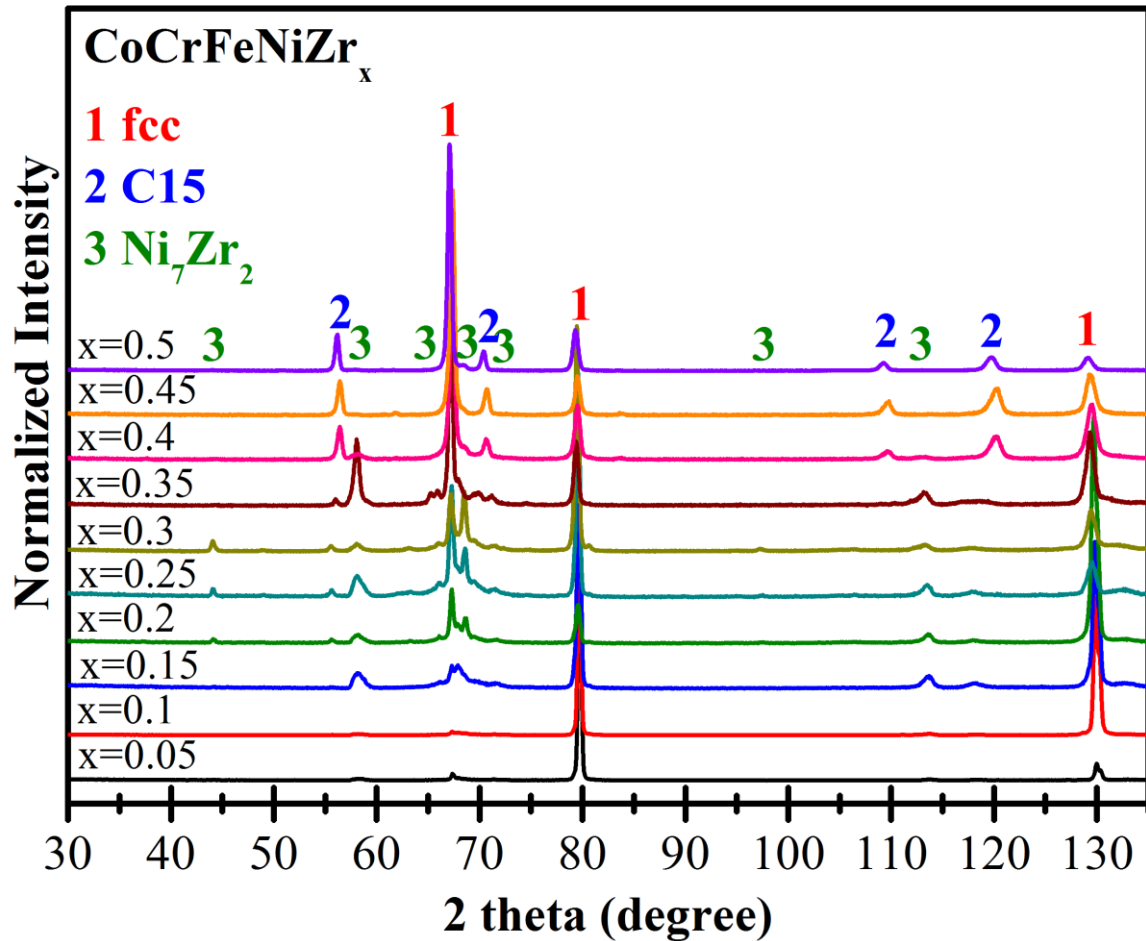
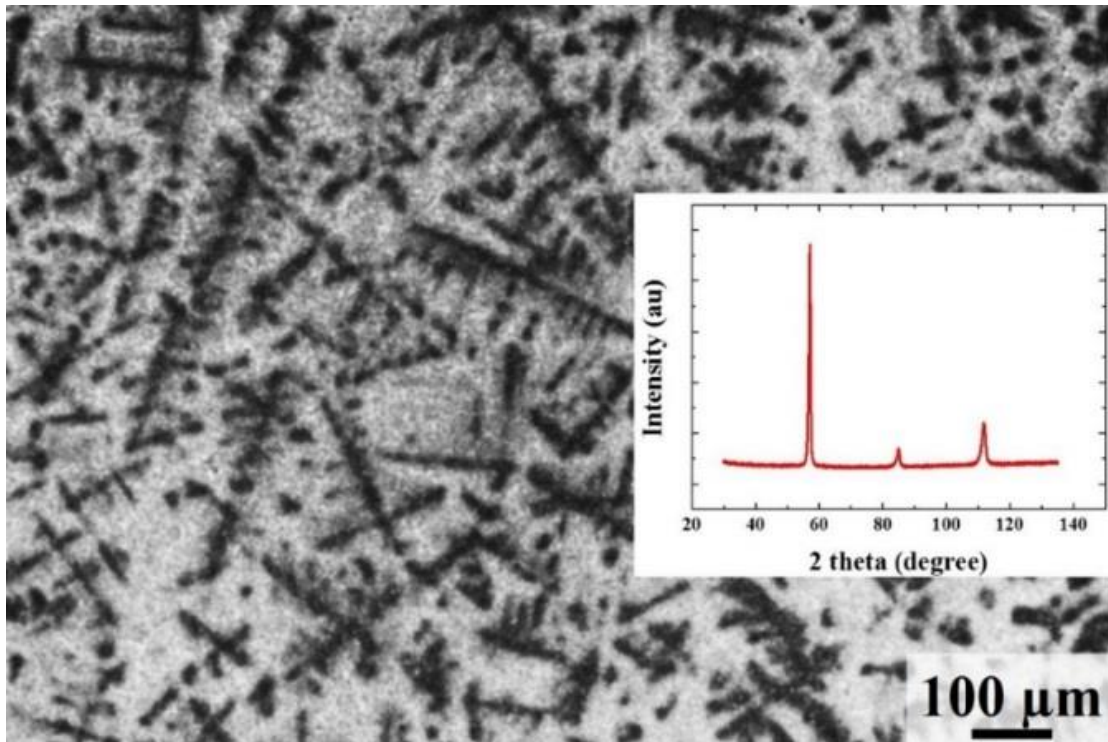


Figure 13: XRD patterns for CoCrFeNiZr<sub>x</sub> alloys, published with permission from AIP.

For  $x=0.05$  and  $0.1$ , the XRD patterns seem to contain mainly the fcc solid solution phase, plus a small amount of the Ni<sub>7</sub>Zr<sub>2</sub> phase. From  $x=0.15$  to  $x=0.4$ , XRD results indicate the existence of three phases, namely the fcc solid solution phase, the Ni<sub>7</sub>Zr<sub>2</sub> phase and the Co<sub>2</sub>Zr-like C15 Laves phase. The amount of the C15 Laves phase at  $x=0.15$  and the amount of the Ni<sub>7</sub>Zr<sub>2</sub> phase at  $x=0.4$  are negligible judging from their weak peak intensities. For  $x=0.45$  and  $0.5$ , the XRD patterns show only two phases, the fcc solid solution phase and the C15 Laves phase. The XRD results indicate that Zr has almost no solid solubility in CoCrFeNiZr<sub>x</sub> alloys. In short, The Md parameter, better than the current approaches, can accurately predict the solid solubility, or the phase boundary between the fcc solid solution and intermetallic compounds in HEAs.

## 5.2 VEC and RHEAs

Figure 14 shows the backscattered electron SEM micrograph of the as-cast alloy with a dendritic structure. Regardless of heavy alloying, XRD pattern indicates a single-phase bcc structure, with all three main peaks identified. Constituent elements have bcc crystal lattices just below their melting temperatures. Binary alloying of Nb with Ta results in a bcc structure with a continuous solid solution in the entire composition range [120]. Hf, Zr and Ti also form continuous solid solutions with each other, but hexagonal close packed (hcp) crystal structure is also reported at lower temperatures due to polymorphic transformations. For the  $\text{Hf}_{0.5}\text{Nb}_{0.5}\text{Ta}_{0.5}\text{Ti}_{1.5}\text{Zr}$  alloy, the formation of hcp phase is kinetically restricted and only bcc phase is formed which can be referred to the high configurational entropy and slow diffusivity of elements in the multicomponent alloys [7, 121].



**Figure 14: As-cast microstructure with a typical dendritic and inter-dendritic morphology; the alloy is of single bcc phase, as shown from the XRD inset, published with permission from AIP.**

It is necessary to point out that single phase solid solution is a pre-condition to justify the *VEC* concept for ductilizing RHEA in order to avoid any influence from the secondary phases. Table 12 lists nine different RHEAs containing elements from group IV, V and VI and their corresponding *VEC* values. We have tried to cover a range of alloys based on their *VEC*, with the minimum value of 4.25 and the maximum of 5.5. Among them, three are ductile RHEAs (tensile elongation > 5%) while six are brittle. These are all reported to be single phase bcc alloys.

**Table 12: Refractory HEAs and their corresponding VEC.**

Alloy system	VEC	Reference
HfNbTiZr	4.25	[73]
Hf <sub>0.5</sub> Nb <sub>0.5</sub> Ta <sub>0.5</sub> Ti <sub>1.5</sub> Zr	4.25	[This work]
HfNbTaTiZr	4.4	[33]
HfMoTaTiZr	4.6	[122]
HfMoNbTaTiZr	4.67	[122]
HfMoNbTiZr	4.6	[123]
MoNbTaVW	5.4	[11, 15]
MoNbTaW	5.5	[11, 15]
MoNbTaV	5.25	[124]

A new RHEA of type, Hf<sub>0.5</sub>Nb<sub>0.5</sub>Ta<sub>0.5</sub>Ti<sub>1.5</sub>Zr, has been designed, based on our intention to develop intrinsically ductile RHEAs following the electron theory, i.e. to keep *VEC* low. Ductile RHEAs have a *VEC* ≤ 4.4, while all brittle alloys have a *VEC* ≥ 4.6. With the related information of nine alloys, it is perhaps not convincing enough to conclude that there exists a threshold *VEC* of ~ 4.5 below which intrinsic ductility can be achieved in RHEAs. However, decreasing *VEC* in RHEAs by controlled alloying has indeed proven effective in ductilizing RHEAs which is further illustrated in Fig. 15.

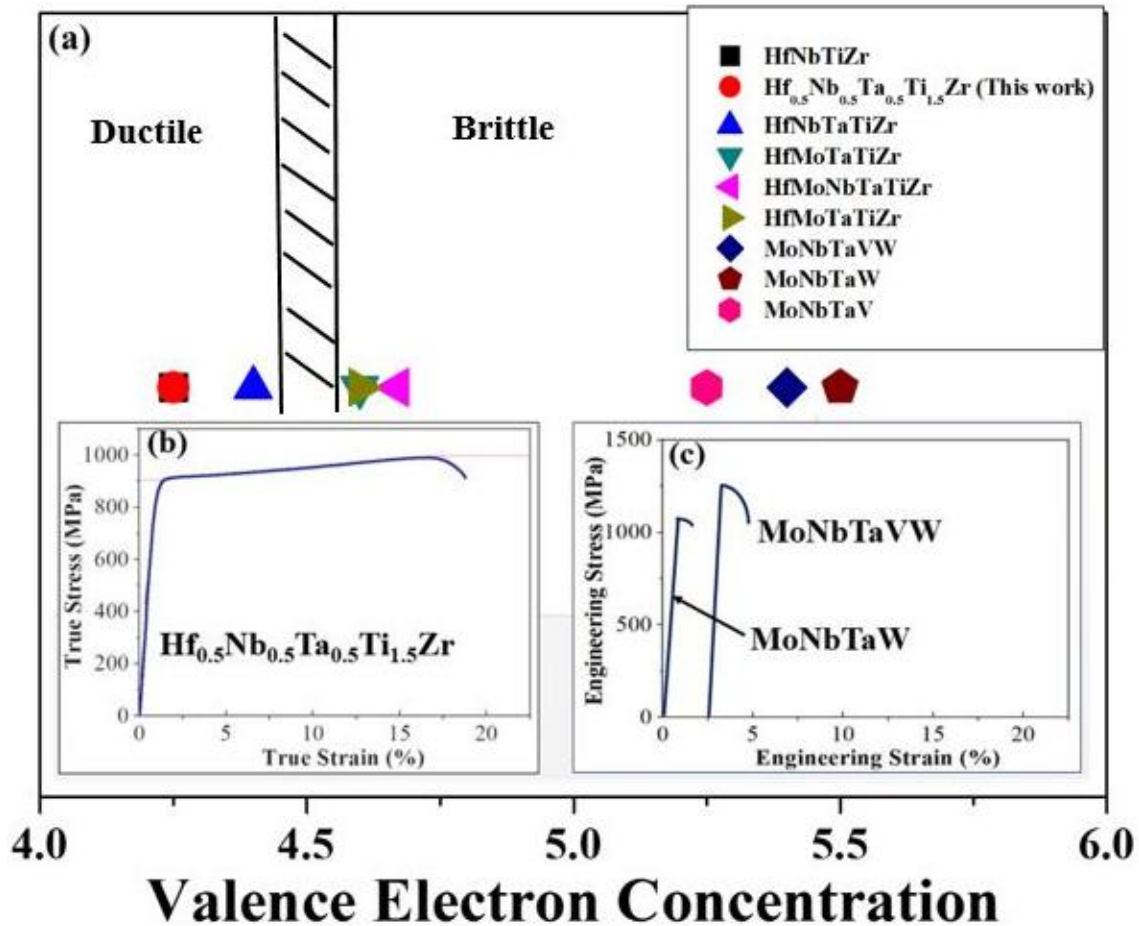
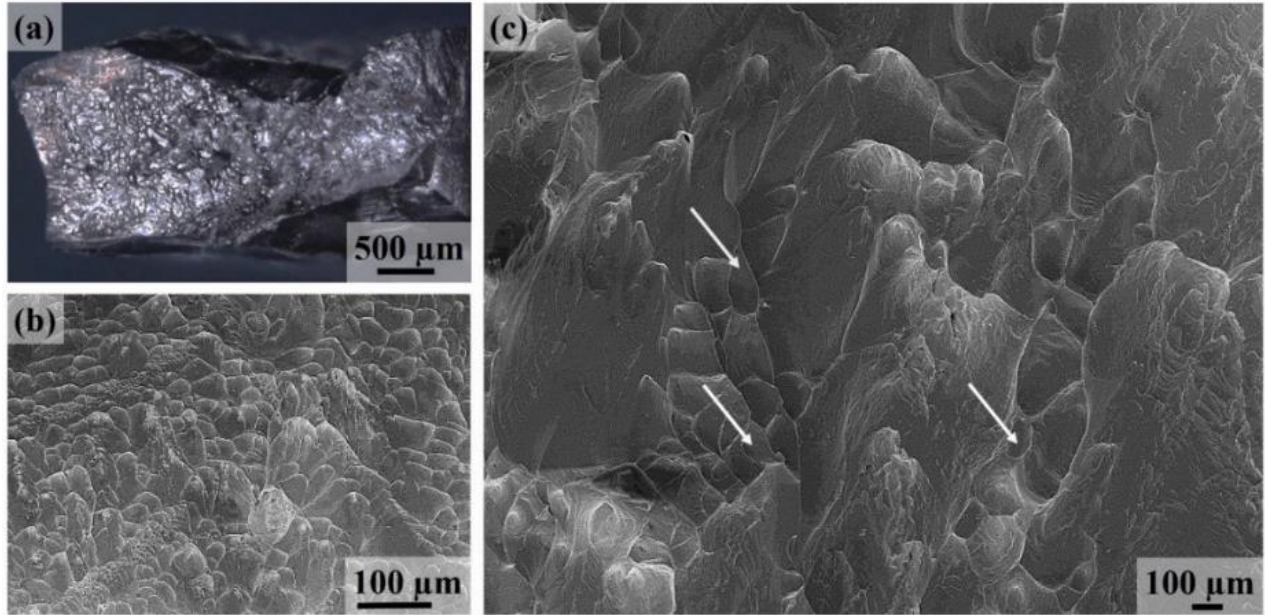


Figure 15: Plot of VEC for different RHEAs (a); Three of the alloys with lower VEC are ductile among which, two are reported and one is from this work also complemented by tensile stress-strain graph for Hf<sub>0.5</sub>Nb<sub>0.5</sub>Ta<sub>0.5</sub>Ti<sub>1.5</sub>Zr (b); Alloys with higher VEC are reportedly brittle alloys and is shown by engineering stress- strain compression curves of MoNbTaVW and MoNbTaW alloys (c) [11, 15]. (c) is reproduced with permission from Institute for Scientific Information.

Interestingly, there exists a clearly shift in the material behavior based upon *VEC*, i.e. RHEAs with lower *VEC* show a combination of high fracture strength and high ductility, as shown in the tensile test result in Fig. 15 (b), while at higher *VEC* the materials are brittle, as shown in the compression testing result in Fig. 15 (c) [11, 15]. Alloying additions can alter the Fermi level, and therefore tune the corresponding intrinsic failure mode and critical strain for the shear instability.

Lowering the number of valence electrons shifts the Fermi level down relative to the band structure, so less strain is required and the shear instability occurs much earlier. Based upon the results, it is suggested that intrinsically ductile RHEAs can be designed by controlling VEC through alloying. It has to be emphasized that the strategy is essentially directed to bcc solid solutions. The as-cast  $\text{Hf}_{0.5}\text{Nb}_{0.5}\text{Ta}_{0.5}\text{Ti}_{1.5}\text{Zr}$  alloy has a room temperature tensile strength of 990 MPa and an elongation of 18.8%, in the true stress/strain condition. High fracture strength of this RHEA is referred to the strong bonding obtained from the refractory elements. Also, plastic strain to such extent is not usually found among bcc HEAs. The yield stress (determined by shifting the linear elastic curve to 0.2% strain) is determined to be 903 MPa, and the Vickers hardness is found to be 301 HV. It is important to comment here that the mechanical properties of the as-cast RHEA can be further modified by thermo-mechanical treatments which will make these alloys even more attractive. The top-view of the fractured tensile specimen as observed by stereomicroscopy is shown in Fig. 16 (a), which indicates plastic deformation and necking-like behaviour. It is known that most of the common structural alloys fail through microvoid coalescence, where excessive load leads to fracture. The formation of microvoids is associated with dislocation pile-ups, grain boundaries, inclusions or due to secondary particles/phases, leading to dimple rupture for the case of ductile materials. In our case, since we are dealing with single phase alloys, microvoid formation due to secondary particles will be ruled out. It is also known that the direction of maximum stress applied has an influence on the shape of dimples formed. Under tensile testing, equiaxed and elongated dimples pointing towards fracture origin can be formed. This seems to be the case in the fracture morphology for  $\text{Hf}_{0.5}\text{Nb}_{0.5}\text{Ta}_{0.5}\text{Ti}_{1.5}\text{Zr}$  alloy, as shown in Fig. 16 (b), i.e., both equiaxed and elongated dimples are present. Large and smaller dimples are visible, but they seem to be rather shallow as shown in Fig. 16 (c).



**Figure 16: Fractured surface of tensile specimen  $\text{Hf}_{0.5}\text{Nb}_{0.5}\text{Ta}_{0.5}\text{Ti}_{1.5}\text{Zr}$  (a) Stereomicroscopic image of the fracture surfaces with signs of necking like behaviour; (b) SEM image with both equiaxed and elongated dimples in different regions; (c) SEM image at higher magnification image showing cup shaped dimples marked by arrows, published with permission from AIP.**

It is significant to note here that the density of RHEA  $\text{Hf}_{0.5}\text{Nb}_{0.5}\text{Ta}_{0.5}\text{Ti}_{1.5}\text{Zr}$  was measured to be  $8.13 \text{ g/cm}^3$  using the Archimedes' principle, and is comparable to the density of current Ni-based superalloys and lower than other RHEAs. The usual perception of most of the RHEAs is their rather high densities, such as  $\text{MoNbTaVW}$  ( $12.36 \text{ g/cm}^3$ ) and  $\text{MoNbTaW}$  ( $13.8 \text{ g/cm}^3$ ),  $\text{HfNbTaTiZr}$  ( $9.94 \text{ g/cm}^3$ ),  $\text{HfMoTaTiZr}$  ( $10.24 \text{ g/cm}^3$ ) and  $\text{HfMoNbTaTiZr}$  ( $9.97 \text{ g/cm}^3$ ). Based on the estimated melting point of  $2055 \text{ }^\circ\text{C}$  by rule of mixture,  $\text{Hf}_{0.5}\text{Nb}_{0.5}\text{Ta}_{0.5}\text{Ti}_{1.5}\text{Zr}$  certainly has potential to compete with current superalloys. Further optimization of both room and elevated temperature properties while keeping the density relatively low will certainly enable RHEAs to become competitive high-temperature alloys to superalloys. A comparison of yield strength versus density of RHEA and of major material classes is given in Fig. 17 [125]. There are

materials which have higher yield strength than current RHEA, but still, one should not forget that  $\text{Hf}_{0.5}\text{Nb}_{0.5}\text{Ta}_{0.5}\text{Ti}_{1.5}\text{Zr}$  is a single phase material with as good strength/density values as most of the current materials, and in some cases they outperform current ones. Immobile structures may utilize high density materials, but aerospace industry has a constant demand for low-density metallic alloys in high-temperature thermal protection systems, especially load-bearing structures. Therefore, we have a clear motivation for exploring HEAs composed of constituents that can result in alloys with optimal mechanical properties, high melting temperatures and densities reduced as much as possible.

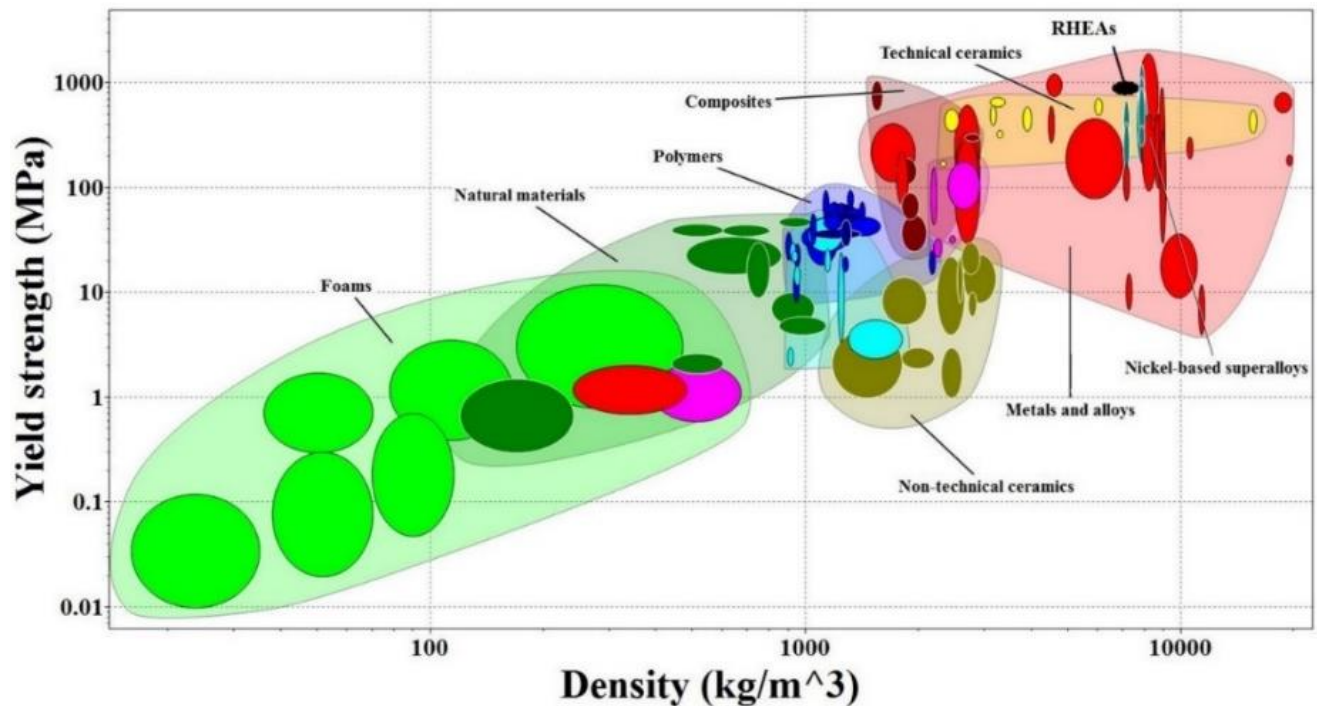


**Figure 17: Ashby map showing yield strength as a function of density for  $\text{Hf}_{0.5}\text{Nb}_{0.5}\text{Ta}_{0.5}\text{Ti}_{1.5}\text{Zr}$  in relation to the wide range of material systems. The high yield strength combined with rather low density makes RHEAs potential materials for future applications.**

To conclude, we have employed *VEC* to design a new ductile RHEA,  $\text{Hf}_{0.5}\text{Nb}_{0.5}\text{Ta}_{0.5}\text{Ti}_{1.5}\text{Zr}$ , with a yield stress of 903 MPa, a fracture stress of 990 MPa, a density of 8.13 g/cm<sup>3</sup> and an elongation of 18.8%. This material has superior properties compared to previously developed ductile RHEAs. It is proposed that lowering the *VEC*, which can be controlled by adjusting the alloy composition, could be a valid strategy for ductilizing single phase bcc RHEAs comprising of elements from group IV, V and VI elements. This approach has so far been validated by three ductile materials with lower *VEC*:  $\text{HfNbTiZr}$ ,  $\text{Hf}_{0.5}\text{Nb}_{0.5}\text{Ta}_{0.5}\text{Ti}_{1.5}\text{Zr}$  and  $\text{HfNbTaTiZr}$ , and six brittle materials with rather higher *VEC*:  $\text{HfMoNbTiZr}$ ,  $\text{HfMoNbTaTiZr}$ ,  $\text{MoNbTaVW}$ ,  $\text{MoNbTaW}$ ,  $\text{MoNbTaV}$  and  $\text{HfMoTaTiZr}$ . This outcome of alloy design using *VEC* is certainly exciting, as it opens up the prospects of using a simple and single parameter to design ductile RHEAs, which have been studied quite extensively recently.

### 5.3 Thermomechanically treated $\text{Hf}_{0.5}\text{Nb}_{0.5}\text{Ta}_{0.5}\text{Ti}_{1.5}\text{Zr}$

Thermomechanical treatments (cold rolling and annealing) were also used to further improve the mechanical performance of the as-cast  $\text{Hf}_{0.5}\text{Nb}_{0.5}\text{Ta}_{0.5}\text{Ti}_{1.5}\text{Zr}$ . Figures 18(a)–(c) are the representative EBSD maps of sample A, B and C, obtained after annealing the cold-rolled samples. The average grain size of sample A, B and C is 124 μm, 160 μm and 195 μm respectively. The grain sizes are dependent on the annealing temperature, time and extent of cold work [126], and increases with the annealing time and temperature, as is observed for the current alloys. Secondary phases were not observed at grain boundaries or inside the grains of the annealed alloys.

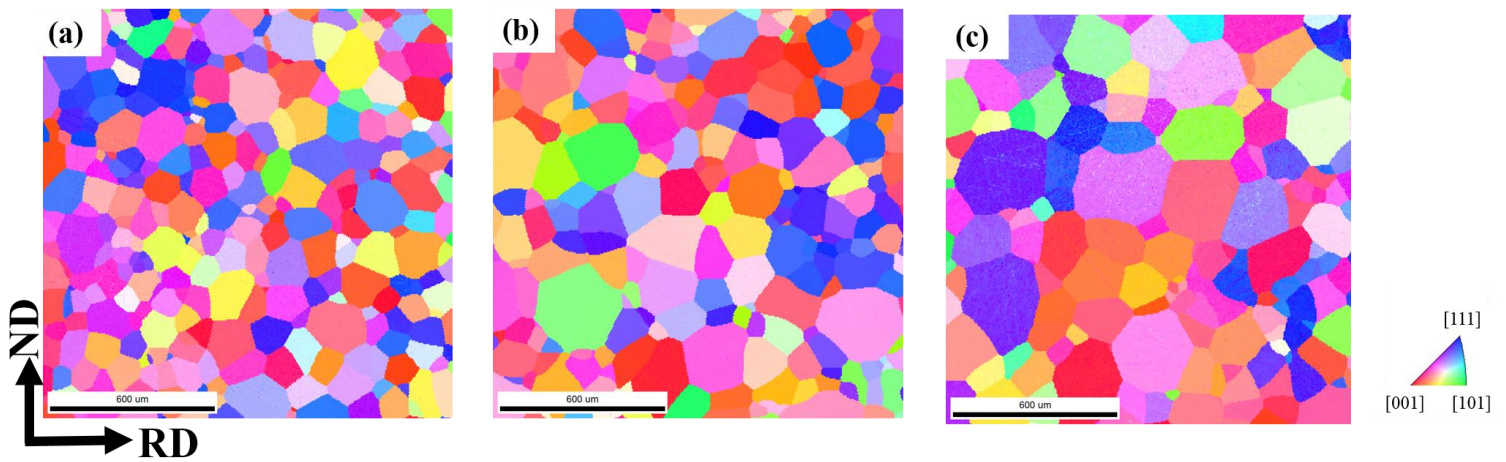


**Figure 18: Rolling-direction EBSD IPF figures of  $\text{Hf}_{0.5}\text{Nb}_{0.5}\text{Ta}_{0.5}\text{Ti}_{1.5}\text{Zr}$  alloy with different grain size for sample A (a), sample B (b), and sample C (c).**

To determine the role of grain size and tensile properties of the current HEAs, tensile testing was carried out on the annealed samples A, B and C. Figure 19 shows their true stress–strain curves. The yield strengths of samples A, B, and C are 1100, 1080 and 1050 MPa; while the ultimate tensile strengths are 1120, 1105, and 1080 MPa, respectively, higher as compared to the as-cast state. The corresponding true strains for samples A, B, and C are 7.2 %, 7.6 % and 14.4 %, respectively.

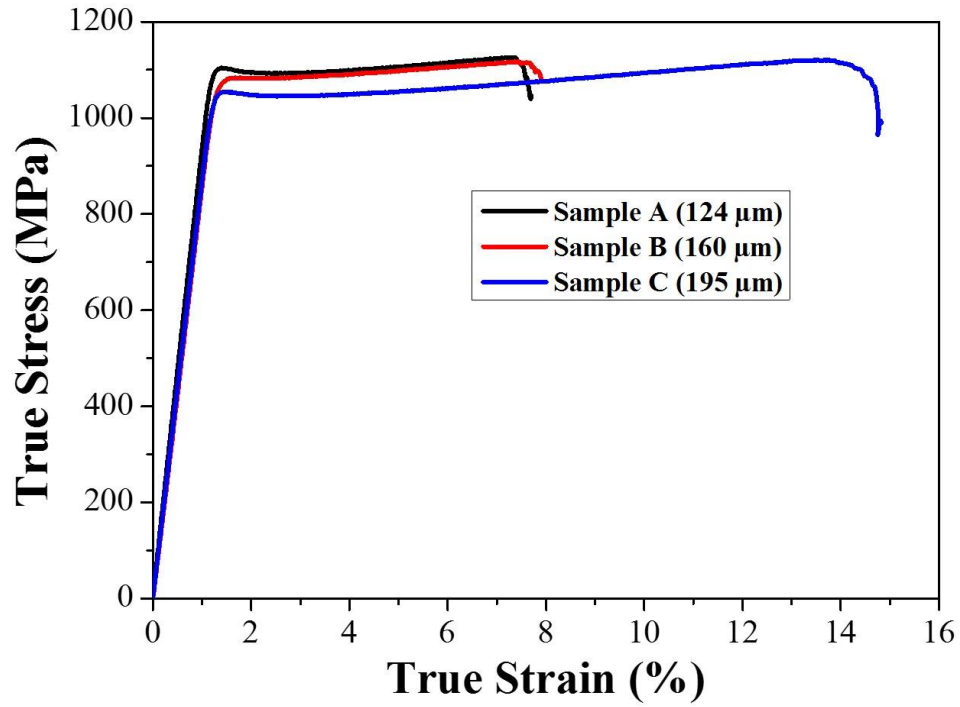


**Figure 19: True tensile stress–strain curves of  $\text{Hf}_{0.5}\text{Nb}_{0.5}\text{Ta}_{0.5}\text{Ti}_{1.5}\text{Zr}$  alloy with different grain size.**

#### **5.4 Oxidation studies for ductile RHEA**

Fig. 20 shows the weight change per unit area versus time curves for the ductile  $\text{Hf}_{0.5}\text{Nb}_{0.5}\text{Ta}_{0.5}\text{Ti}_{1.5}\text{Zr}$  RHEA that was oxidized in the temperature range of 600-1100 °C.

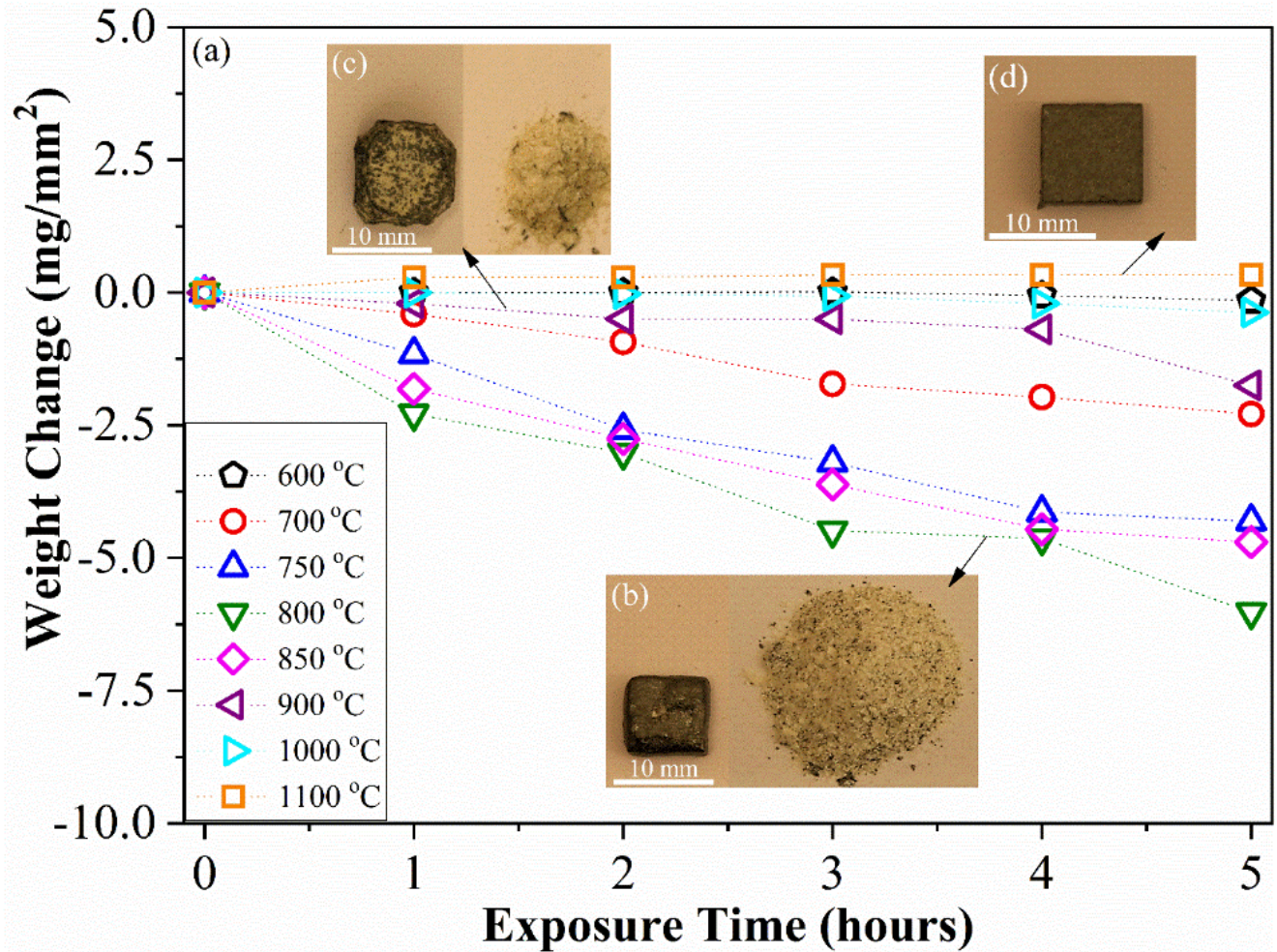


**Figure 20: (a) Weight change as a function of exposure time from 600 to 1100 °C for  $\text{Hf}_{0.5}\text{Nb}_{0.5}\text{Ta}_{0.5}\text{Ti}_{1.5}\text{Zr}$ . The inset images (b) and (c) shows the remaining bulk alloys and spalled-off powders after 5h of oxidation at 800 °C and 900 °C, respectively, and (d) shows the alloy after 5h of oxidation at 1100 °C, without any indication of pesting, published with permission from Elsevier Ltd.**

Two distinctive oxidation behaviors can be observed. At temperatures from 600-1000 °C, the RHEA displays accelerated oxidation evidenced by material gradually disintegrating into powders, while at temperatures higher than 1000 °C, the alloy retains its shape without any noticeable powder formation. For the first case, almost at all temperatures continuous weight loss (only the bulk specimen was weighed, not including the spalled-off powders) is observed, and the

spallation from the sample surface continuously exposes fresh surfaces to oxidation and eventually leads the alloy to disintegrate into powders, known as pesting. Pesting is most severe for the current RHEA oxidized at 800 °C, with a drastic weight change of  $-6.022 \text{ mg/mm}^2$  after 5h as showcased in Fig. 20(a), while Fig. 20(b) clearly shows the remaining bulk material and spalled-off powders. Above and below 800 °C, i.e., at 700 and 750 °C, and 850 and 900 °C, pesting is also found but is less severe compared to at 800 °C, seen from Fig. 20(c) for example, on the specimen oxidized at 900 °C for 5h, where less amount of powders are spalled off from the bulk alloy. Noticeably, the weight changes at 600 and 1000 °C are insignificant, and there is even an initial positive weight change for oxidation at 600 °C up to 3h, but further exposure at this temperature results in negative weight change, despite the weight change is merely  $-0.150 \text{ mg/mm}^2$  after 5h. Although no positive weight change is seen for 1000 °C, the weight change after 5h is only  $-0.375 \text{ mg/mm}^2$ . These rather small weight changes as compared to the ones at other temperatures could have been confused with typical weight loss during oxidation, therefore, extended oxidation tests for 24h were carried out and they confirmed pesting would occur at both 600 and 1000 °C. Those extended oxidation results are not included here though, and only the weight change results up to 5h are presented, to keep the same exposure time for all temperatures. When the exposure temperature was raised to 1100 °C, a sharp change of oxidation behavior is noted in that the alloy experiences continuous weight gain without any sign of pesting, as evidenced by Fig. 20(d). Oxidation tests were also carried out at 300, 400 and 500 °C and no pesting was observed at these low temperatures, and those results are also not included here. Summarizing the isothermal oxidation tests, the oxidation behavior for  $\text{Hf}_{0.5}\text{Nb}_{0.5}\text{Ta}_{0.5}\text{Ti}_{1.5}\text{Zr}$  RHEA is strongly dependent on the temperature and also time, and most importantly the catastrophic oxidation, pesting, is observed to occur in the temperature range of 600-1000 °C. Short term oxidation tests were also carried out, to get information on the initial oxides formation

and their growth, which could help to understand the initiation of pitting. Figure 21 shows the side- and top-view of the surface from the specimen that was oxidized at 800 °C for 10 min, which already exhibits spallation and cracking of oxide layers.

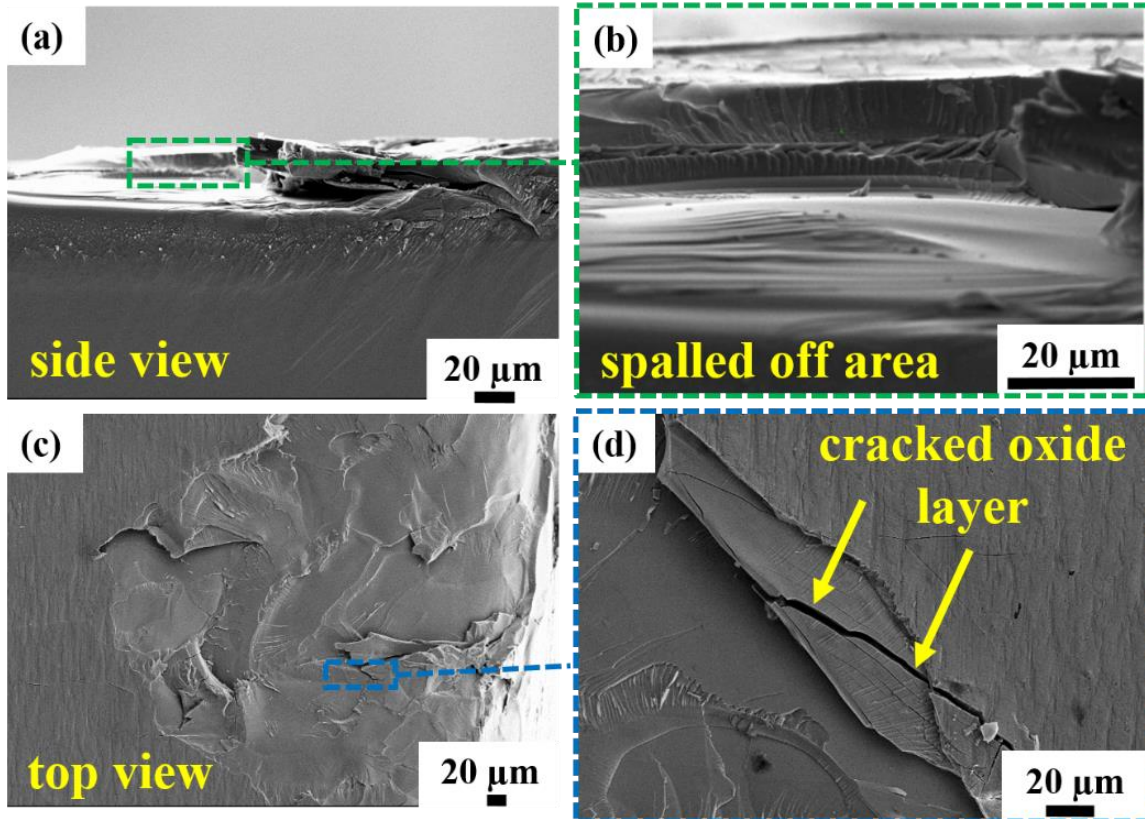


**Figure 21:** (a) and (b) Side-view of the bulk Hf<sub>0.5</sub>Nb<sub>0.5</sub>Ta<sub>0.5</sub>Ti<sub>1.5</sub>Zr alloy after short-term oxidation at 800 °C for 10 minutes (untreated); (c) and (d) Top-view of the surface after spallation, with cracks on the oxide layer indicated by arrows, published with permission from Elsevier Ltd.

Figure 21(a) and 21(b) clearly capture the early spallation of oxide layers, which leaves a quite smooth surface. Cracks in the oxides can be seen from the top-view images that are shown in Figs. 21(c) and 21(d), the propagation of which is believed to lead to the spallation. On the other hand, the oxygen ingress can start from the fresh surface and move into the bulk alloy through the cracks, and simultaneously metal atoms can also move towards the surface through the cracks.

When these metal atoms arrive at the surface, they come into reaction with oxygen, forming the oxides. The oxides grow and the stresses build up due to the increasing mismatch in volume expansion between the oxides and the base alloy, leading to cracking and then spallation, and the cycle continues. This scenario is essentially how pesting occurs in the current RHEA. In order to prevent pesting within HEAs, we tried to identify the role of individual elements on the overall oxidation and pesting. It started with the quaternary alloys  $\text{Nb}_{0.5}\text{Ta}_{0.5}\text{Ti}_{1.5}\text{Zr}$  and  $\text{Hf}_{0.5}\text{Nb}_{0.5}\text{Ta}_{0.5}\text{Ti}_{1.5}$  by removing Hf and Zr, respectively, from the parent  $\text{Hf}_{0.5}\text{Nb}_{0.5}\text{Ta}_{0.5}\text{Ti}_{1.5}\text{Zr}$  alloy, since Zr (1.602 Å) and Hf (1.578 Å) have not only high oxygen affinity, but also larger atomic radii as compared to Nb (~1.429 Å), Ti (~ 1.462 Å) and Ta (~ 1.43 Å) [127]. Both  $\text{Nb}_{0.5}\text{Ta}_{0.5}\text{Ti}_{1.5}\text{Zr}$  and  $\text{Hf}_{0.5}\text{Nb}_{0.5}\text{Ta}_{0.5}\text{Ti}_{1.5}$  alloys upon oxidation exhibited the pesting behavior in the pesting temperature range for the  $\text{Hf}_{0.5}\text{Nb}_{0.5}\text{Ta}_{0.5}\text{Ti}_{1.5}\text{Zr}$  RHEA, and disintegrated into powders (results not shown here). Later, both Zr and Hf were removed from the parent  $\text{Hf}_{0.5}\text{Nb}_{0.5}\text{Ta}_{0.5}\text{Ti}_{1.5}\text{Zr}$  alloy. The Zr and Hf removed ternary  $\text{Nb}_{0.5}\text{Ta}_{0.5}\text{Ti}_{1.5}$  alloy did not show any pesting.

## **5.5 Aluminizing studies for ductile RHEA**

### **5.5.1 Oxidation resistance for aluminized $\text{Hf}_{0.5}\text{Nb}_{0.5}\text{Ta}_{0.5}\text{Ti}_{1.5}\text{Zr}$**

Figure 22 shows the effect of different aluminizing conditions (pack compositions and aluminizing time in this case, as given in Table 9) on the oxidation resistance for aluminized  $\text{Hf}_{0.5}\text{Nb}_{0.5}\text{Ta}_{0.5}\text{Ti}_{1.5}\text{Zr}$ . Seen from Fig. 22(b), the specimen S1-NiAl60-5h-O experiences pesting as evidenced by material disintegration into powders, a sign indicating that the aluminized coating was not protective. However, the amount of powder produced is much less compared to the un-aluminized as-cast RHEA, under the same oxidation condition [128]. It indicates that the aluminized layer does improve the oxidation resistance by limiting the oxygen penetration into

the bulk of the material, but the improvement simply slows down but does not prevent pesting. Pesting is most severe for the specimen S1-NiAl54-5h-O, as is shown in Fig. 22(f) where nearly the whole bulk material disintegrates into powders. Noticeably, the specimen S1-Al,Cr-5h-O shows no indication of pesting, as seen in Fig. 22(h). By reducing the aluminizing time from 5h to 2h, the specimen S1-NiAl60-2h-O (Fig. 22(d)) exhibits more significant pesting compared to S1-NiAl60-5h-O (Fig.22(b)), while pesting is observed in the specimen S1-Al,Cr-2h-O (Fig. 22(j)). Therefore, the combination of pact composition and aluminizing time can be optimized for improving the oxidation resistance of  $\text{Hf}_{0.5}\text{Nb}_{0.5}\text{Ta}_{0.5}\text{Ti}_{1.5}\text{Zr}$ , with the possibility of avoiding pesting. The results shown here also indicate that compared to low Al activity, high Al activity and longer aluminizing time are the advantageous aluminizing conditions for improving the oxidation resistance for  $\text{Hf}_{0.5}\text{Nb}_{0.5}\text{Ta}_{0.5}\text{Ti}_{1.5}\text{Zr}$ .

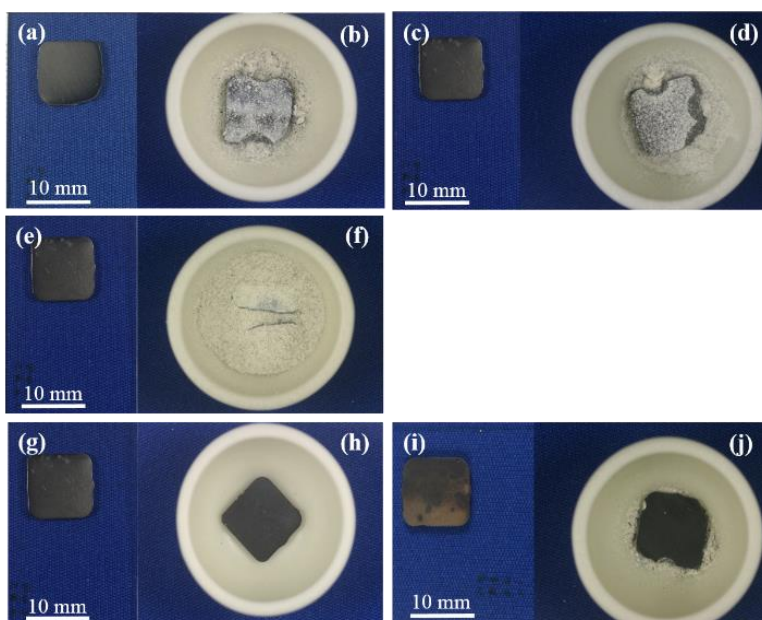


**Figure 22:** (a) and (b) show the as-aluminized specimen S1-NiAl60-5h-A and oxidized specimen S1-NiAl60-5h-O; Similarly, (c) and (d) for S1-NiAl60-2h-A and S1-NiAl60-2h-O; (e) and (f) for S1-NiAl54-5h-A and S1-NiAl54-5h-O; (g) and (h) for S1-Al,Cr-5h-A and S1-Al,Cr-5h-O; (i) and (j) for S1-Al,Cr-2h-A and S1-Al,Cr-2h-O (corresponding to Table 9).

Figures 23 (a) and (b) show the cross-sectional microstructure of the specimens S1-Al,Cr-5h-A and S1-Al,Cr-5h-O. The aluminized layer contains a few cracks but maintains a good contact with the substrate. In both as-aluminized and oxidized specimens, an outer aluminum rich thin layer and beneath it, a thick inter-diffusion zone (IDZ) are observed. After oxidation, the substrate and IDZ experience diffusion into each other and the outward diffusion of Zr into the IDZ is most significant, which is due to Zr having the most negative enthalpy of mixing with Al as compared to other constituent elements in the substrate (Fig. 23 (g)). Noticeably, a dense and intact oxide layer is formed as seen from Figs. 23 (b) and (i), although cracks are still present. The oxide seems to also fill in the cracks, which might help to prevent oxygen penetration into the substrate.

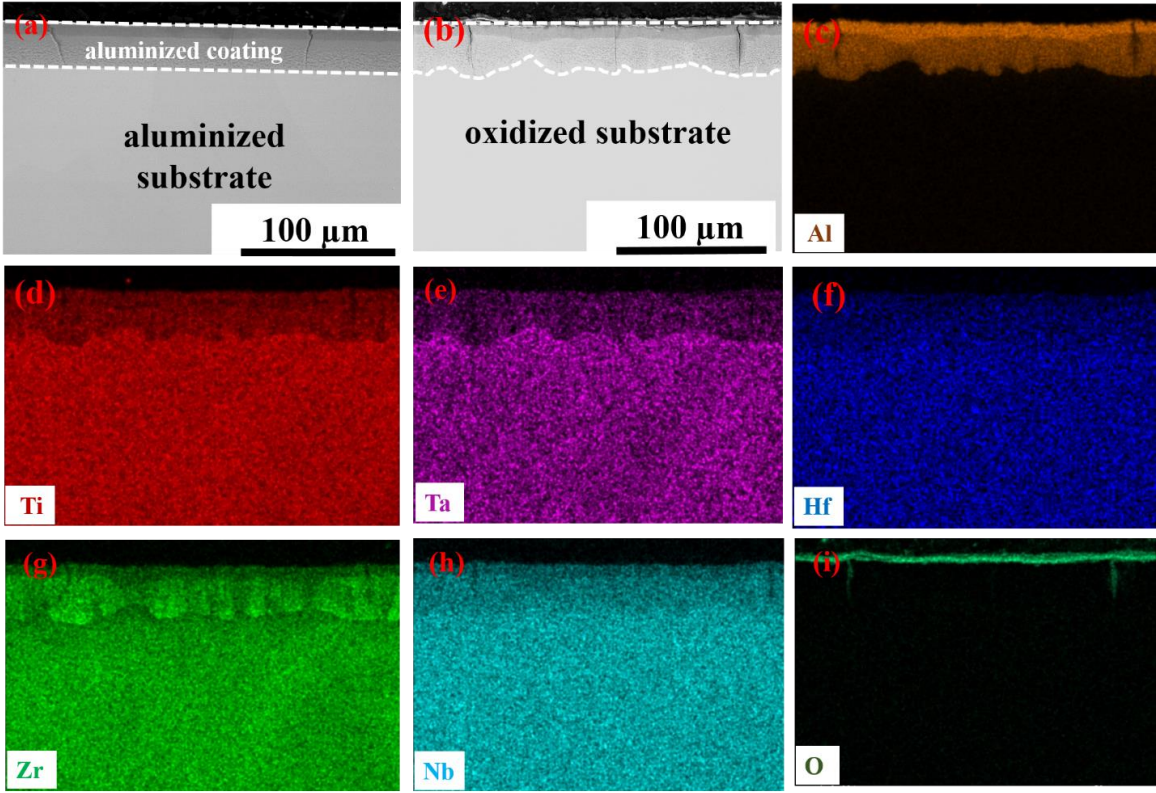


**Figure 23: (a) and (b) Cross-sectional microstructure of the specimens S1-Al,Cr-5h-A and S1-Al,Cr-5h-O. SEM-EDS elemental maps for the S1-Al,Cr-5h-O specimen are given shown in (c)-(i).**

### 5.5.2 Oxidation resistance for aluminized $\text{Al}_{0.5}\text{Cr}_{0.25}\text{Nb}_{0.5}\text{Ta}_{0.5}\text{Ti}_{1.5}$

To improve the oxidation resistance of  $\text{Al}_{0.5}\text{Cr}_{0.25}\text{Nb}_{0.5}\text{Ta}_{0.5}\text{Ti}_{1.5}$ , aluminizing is also applied to it with the detailed aluminizing conditions given in Table 10. Figures 24 (a), (c) and (e) show the microstructure of aluminized layers in specimens S2-NiAl54-5h-A, S2-NiAl60-2h-A and S2-Al,Cr-2h-A. In all specimens, a cover layer, and a diffusion zone underneath it are observed. After oxidation, the microstructures of aluminized layers in specimens S2-NiAl54-5h-O, S2-NiAl60-2h-O and S2-Al,Cr-2h-O are shown in Figs. 24(b), (d) and (f). The thickness of the cover layer is thinnest for S2-NiAl54-5h-O while thickest for S2-Al,Cr-2h-O.

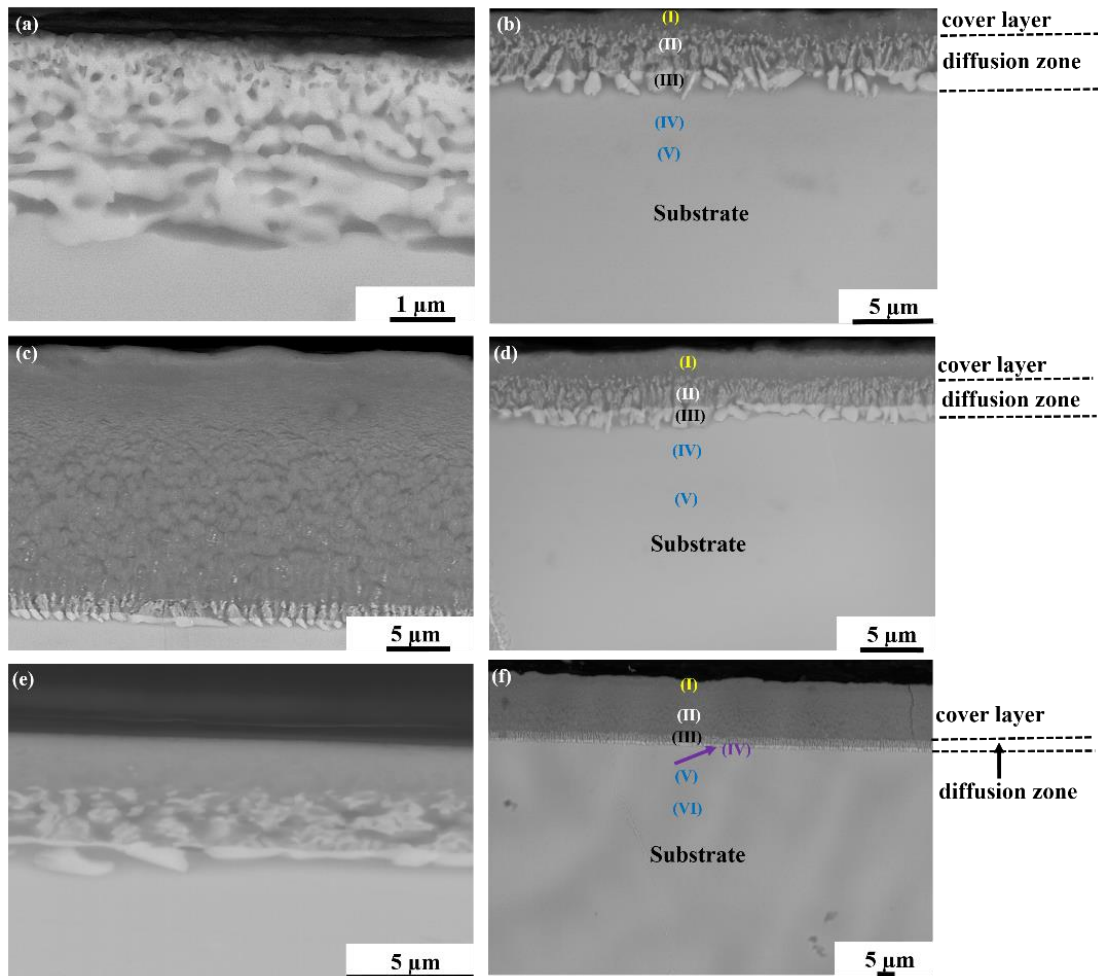


**Figure 24:** Cross sections of specimens S2-NiAl54-5h-A, S2-NiAl60-2h-A and S2-Al,Cr-2h-A are shown in (a),(c) and (e), while those for specimens S2-NiAl54-5h-O, S2-NiAl60-2h-O and S2-Al,Cr-2h-O are shown in (b), (d) and (f), respectively.

The microstructures within the diffusion zones are rather complex and consist of multiple phases with varying morphologies. The understanding of the phases formed in these diffusion zones requires detailed transmission electron microscopy work, and is not pursued here. SEM-EDS analyses in Table 13 indicate that all constituent elements in the substrate are present throughout the aluminized coating.

**Table 13: SEM-EDS analysis for the substrate and aluminized layers for specimens S2-NiAl54-5h-O, S2-NiAl60-2h-O and S2-Al,Cr-2h-O. The corresponding regions are shown in Fig. 13(b), (d) and (f).**

Composition	Element (at. %)					
Region	Al	Cr	Nb	Ta	Ti	O
<b>Sample S2-NiAl54-5h-O</b>						
(I)	12.3	3.0	5.4	4.4	6.3	68.6
(II)	57.2	4.9	7.6	5.3	25.0	-
(III)	28.4	8.2	15.0	12.4	32.8	3.2
(IV)	14.7	6.4	12.2	10.5	35.1	21.1
(V)	15.6	7.0	14.5	12.7	42.0	8.2
<b>Sample S2-NiAl60-2h-O</b>						
(I)	70.0	0.6	7.5	4.2	12.5	5.2
(II)	53.0	5.4	7.6	7.2	21.0	5.8
(III)	32.1	3.6	14.2	13.3	29.0	7.8
(IV)	17.2	6.3	15.5	15.0	41.2	4.6
(V)	14.4	6.0	16.2	14.9	42.3	6.0
<b>Sample S2-Al,Cr-2h-O</b>						
(I)	70.2	3.7	3.5	4.2	14.2	4.2
(II)	72.9	0.6	4.8	4.8	15.0	1.9
(III)	50.3	8.1	7.6	8.0	23.3	2.7
(IV)	21.7	6.3	12.7	15.3	40.0	4.0
(V)	15.0	7.2	14.9	14.2	44.5	4.0
(VI)	14.1	7.1	15.0	15.5	45.1	3.2

The oxygen contents at regions within the aluminized layer and the substrate are also provided. Oxygen absorption into the substrate indicates the presence of internal oxidation, seen from Table 13, where the effect of aluminizing conditions on inhibiting oxygen penetration can be seen. Comparing the dissolved oxygen content in three specimens, it is observed that the specimen S2-Al,Cr-2h-O has the least oxygen absorption, while the specimen S2-NiAl54-5h-O dissolves most amount of oxygen. The level of oxygen dissolution is directly related to the material embrittlement, which is usually caused by the oxygen diffusion into the grain boundaries, resulting in the weakening of grain boundaries [129]. As a quick test of the level of embrittlement, specimens S2-NiAl54-5h-O, S2-NiAl60-2h-O and S2-Al,Cr-2h-O are subject to bending tests. All three materials show no sign for plastic deformation and fracture quickly upon bending. Fractography for specimens S2-NiAl54-5h-O and S2-NiAl60-2h-O show complete brittle fracture behavior (results not shown here). Interestingly, the fractography for the specimen S2-Al,Cr-2h-O does show regions featured with dimples, hence indication of local ductile fracture, as is shown in Fig. 25 (b) and (c). Therefore, the aluminizing condition for the specimen S2-Al,Cr-2h-O is the optimal one among the three aluminizing conditions that are tried here, but it still needs to be further improved to avoid oxidation induced embrittlement. Again, high Al activity seems to be the advantageous aluminizing condition for improving the oxidation resistance of  $\text{Al}_{0.5}\text{Cr}_{0.25}\text{Nb}_{0.5}\text{Ta}_{0.5}\text{Ti}_{1.5}$ .

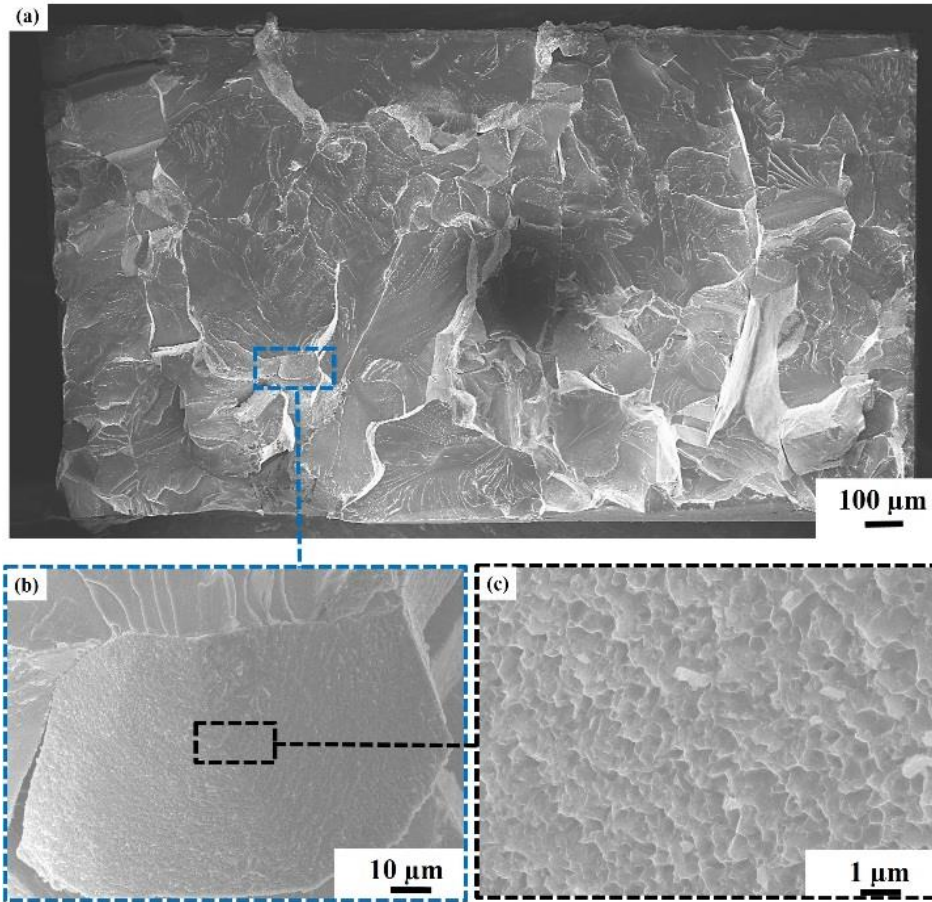


**Figure 25: Fractured surface of the specimen S2-Al,Cr-2h-O. Regions with dimples (ductile fracture) are shown in (b) and (c).**



## 6 Conclusions

### a) *Alloy design*

- **Paper I and II:** The molecular orbital approach previously used to describe the solid solubilities in transition-metal-based terminal solutions is applied first time to HEAs. It was found that the single parameter  $M_d$ , the d-orbital energy level, can well describe the solubility limit HEAs.

### b) *Ductilizing RHEAs*

- **Paper III:** HEAs are considered to be as new types of high-temperature alloys. In this regard, refractory high-entropy alloys (RHEAs), comprising group IV (Ti, Zr, Hf), V (V, Nb, Ta), and VI (Cr, Mo, W) refractory elements have gained lot of attention. However, most existing RHEAs lack room-temperature ductility, similar to conventional refractory metals and alloys. We proposed an alloy design strategy to intrinsically ductilize RHEAs based on the electron theory and more specifically to decrease the number of valence electrons through controlled alloying. A new ductile RHEA, was developed as a proof of concept. These findings shed light on the development of ductile RHEAs for ultrahigh-temperature applications.

### c) *Optimizing mechanical properties and oxidation resistance*

- **Paper IV:** There currently lack efforts to address to two critical issues for RHEAs, i.e., room temperature brittleness and unsatisfactory high-temperature oxidation resistance. The high temperature oxidation behavior of a previously identified ductile  $\text{Hf}_{0.5}\text{Nb}_{0.5}\text{Ta}_{0.5}\text{Ti}_{1.5}\text{Zr}$  RHEA is studied. An accelerated oxidation or more specifically, pesting, in the temperature range of 600-1000 °C is observed for the target RHEA, where the oxidation leads the material to catastrophically disintegrate into powders. The pesting mechanism is studied and is attributed to the failure in forming protective oxide scales accompanied by the accelerated internal oxidation. It is also found out that the simultaneous removal of zirconium and hafnium can eliminate the pesting phenomenon in the alloy. It is believed that pesting can also occur to other equiatomic and non-equiatomic quinary Hf-Nb-Ta-Ti-Zr or quaternary Hf-Nb-Ti-Zr and Hf-Ta-Ti-Zr RHEAs, where all

currently available ductile RHEAs are identified. Research findings provide crucial perspective to the further development of RHEAs as novel high-temperature materials, with balanced room-temperature ductility and high-temperature oxidation resistance.

- **Paper V:** the oxidation resistance of two ductile RHEAs,  $\text{Hf}_{0.5}\text{Nb}_{0.5}\text{Ta}_{0.5}\text{Ti}_{1.5}\text{Zr}$  and  $\text{Al}_{0.5}\text{Cr}_{0.25}\text{Nb}_{0.5}\text{Ta}_{0.5}\text{Ti}_{1.5}$ , are studied after pack cementation at 900 °C using three different pack compositions, with the master alloy being  $\text{Ni}_{40}\text{Al}_{60}$  (at.%),  $\text{Ni}_{46}\text{Al}_{54}$  (at.%) and mixed elemental Al and Cr powders, respectively. Aluminizing, if using the suitable pack cementation parameters, which are the choice of master alloy and aluminizing time in this work, can avoid pesting in  $\text{Hf}_{0.5}\text{Nb}_{0.5}\text{Ta}_{0.5}\text{Ti}_{1.5}\text{Zr}$  and improve the oxidation induced embrittlement in  $\text{Al}_{0.5}\text{Cr}_{0.25}\text{Nb}_{0.5}\text{Ta}_{0.5}\text{Ti}_{1.5}$ . The results obtained show the promise of using aluminizing to further improve the RHEAs toward novel ultrahigh-temperature materials.

## **7 Suggestions for future works**

HEAs cover a very broad range of compositions and microstructures, and efforts have been mostly concentrated to address the composition-microstructure-properties relationship for solid solutions. In this regard, there is limited work reported about the role of intermetallics on the properties of HEAs, especially under tensile loading, for 3d transition metals containing HEAs. The general perception is that intermetallics always embrittle the material, however, for controlled volume fractions and distribution of intermetallics, HEAs have reportedly retained acceptable ductility with increased strength. Exploring further the beneficial role of intermetallics within HEAs can be an important working direction for new structural materials. Precipitation-strengthened multiphase microstructure is one such area of interest within.

For HEAs comprising of refractory metals i.e., RHEAs, their potential lies in high temperature applications. Till date, very limited studies are reported for tensile testing, an important property regarding structural applications requiring further investigation, considering most of the studies have reported compressive ductility and not tensile one. Additionally, oxidation resistance is a serious concern at higher temperatures. Efforts are needed to identify strategies which can help to improve high temperature oxidation resistance, whether it be through alloying or surface modification treatments. Regarding the latter one, aluminizing with appropriate pack cementation parameters to improve the oxidation resistance, holds the promise for further improving the properties of RHEAs as potential high temperature materials, superior than the current state-of-the-art nickel-based superalloys. Recently reported, high-entropy carbides and high-entropy metal diborides have opened up new horizons for further development of ultrahigh temperature materials. These new trends are quite promising and are worthy of further investigations.



## **8 Acknowledgements**

First and foremost, I would like to express gratitude to my supervisor, Associate Professor Sheng Guo, for his continuous support, dedication, patience and encouragement. I am grateful to the Areas of Advance Materials Science, Chalmers University of Technology, for the financial support. During the course of this work, I also had the opportunity to work with bachelors and master students, Thomas Chan Bien Dam, Sarmad Shaba and Muhammad Kurnia Bijaksana. I am thankful to all of them for their contributions.

I would like to thank Samrand Shafeie for all the valuable discussions. I am also obliged to Peter Sotkovszki for his assistance in etching RHEAs. Sincere appreciation for Johan Ahlström in mechanical testing, Eric Tam and Roger Sagdahl for all the troubleshooting, and Håkan Millqvist for the help in the preparation of casting molds. Thanks to Yiming Yao for her assistance in microscopy. Huahai Mao (KTH, Stockholm) for the Thermo-Calc calculations, and Amir Motallebzadeh (Koc University, Turkey) for help on X-ray diffraction tests, are also appreciated.

Lots of appreciation for Assistant Professor Haihui Gary Ruan, host during my exchange visit at The Hong Kong Polytechnic University, Hong Kong. I am also grateful to Hideyuki Murakami, Lu Gan and Te-Kang Tsao from the National Institute for Materials Science, Tsukuba, Japan, for being really kind hosts as well. JSPS and STINT are also appreciated for the financial support regarding my exchange visits.

Thanks to my friends and colleagues at Chalmers, especially Dinesh, Adrianna, Amir and Mahesh, for their support and keeping a friendly working environment.

The deepest appreciations go to my parents, brothers and Sara, for their patience and understanding. It certainly means a lot to me.

**Saad Sheikh  
Gothenburg  
2018**



## References

1. Dimiduk, D.M. and J.H. Perepezko, *Mo-Si-B Alloys: Developing a Revolutionary Turbine-Engine Material*. MRS Bulletin, 2011. **28**(9): p. 639-645.
2. *Aerospace Materials and Material Technologies*. Vol. 1. 2016: Springer, Singapore.
3. Perepezko, J.H., *The hotter the engine, the better*. Science, 2009. **326**(5956): p. 1068-1069.
4. Fleischer, R.L., *High-temperature, high-strength materials- An overview*. Journal of Metals, 1985. **37**(12): p. 16-20.
5. Fine, M.E., L.D. Brown, and H.L. Marcus, *Elastic constants versus melting temperature in metals*. Scripta Metallurgica, 1984. **18**(9): p. 951-956.
6. Buckman Jr, R., *Alloying of refractory metals*. ASM International, Alloying, 1988: p. 419-445.
7. Yeh, J.W., et al., *Nanostructured high-entropy alloys with multiple principal elements: Novel alloy design concepts and outcomes*. Advanced Engineering Materials, 2004. **6**(5): p. 299-303.
8. Cantor, B., et al., *Microstructural development in equiatomic multicomponent alloys*. Materials Science and Engineering A, 2004. **375-377**: p. 213-218.
9. Gali, A. and E.P. George, *Tensile properties of high- and medium-entropy alloys*. Intermetallics, 2013. **39**(0): p. 74-78.
10. Liu, W.H., et al., *Grain growth and the Hall-Petch relationship in a high-entropy FeCrNiCoMn alloy*. Scripta Materialia, 2013. **68**(7): p. 526-529.
11. Senkov, O.N., et al., *Microstructure and room temperature properties of a high-entropy TaNbHfZrTi alloy*. Journal of Alloys and Compounds, 2011. **509**(20): p. 6043-6048.
12. Senkov, O.N., et al., *Mechanical properties of low-density, refractory multi-principal element alloys of the Cr-Nb-Ti-V-Zr system*. Materials Science and Engineering a-Structural Materials Properties Microstructure and Processing, 2013. **565**: p. 51-62.
13. Senkov, O.N., et al., *Low-density, refractory multi-principal element alloys of the Cr-Nb-Ti-V-Zr system: Microstructure and phase analysis*. Acta Materialia, 2013. **61**(5): p. 1545-1557.
14. Senkov, O.N., et al., *Refractory high-entropy alloys*. Intermetallics, 2010. **18**(9): p. 1758-1765.
15. Senkov, O.N., et al., *Mechanical properties of Nb<sub>25</sub>Mo<sub>25</sub>Ta<sub>25</sub>W<sub>25</sub> and V<sub>20</sub>Nb<sub>20</sub>Mo<sub>20</sub>Ta<sub>20</sub>W<sub>20</sub> refractory high entropy alloys*. Intermetallics, 2011. **19**(5): p. 698-706.
16. Senkov, O.N. and C.F. Woodward, *Microstructure and properties of a refractory NbCrMo<sub>0.5</sub>Ta<sub>0.5</sub>TiZr alloy*. Materials Science and Engineering a-Structural Materials Properties Microstructure and Processing, 2011. **529**: p. 311-320.
17. Guo, S. and C.T. Liu, *Phase stability in high entropy alloys: Formation of solid-solution phase or amorphous phase*. Progress in Natural Science: Materials International, 2011. **21**(6): p. 433-446.
18. Ye, Y.F., C.T. Liu, and Y. Yang, *A geometric model for intrinsic residual strain and phase stability in high entropy alloys*. Acta Materialia, 2015. **94**: p. 152-161.
19. Guo, S., et al., *More than entropy in high-entropy alloys: Forming solid solutions or amorphous phase*. Intermetallics, 2013. **41**: p. 96-103.
20. Yeh, J.W., *Recent progress in high-entropy alloys*. Annales De Chimie-Science Des Materiaux, 2006. **31**(6): p. 633-648.

21. Wu, W.H., C.C. Yang, and J.W. Yeh, *Industrial development of high-entropy alloys*. *Annales De Chimie-Science Des Materiaux*, 2006. **31**(6): p. 737-747.
22. MacDonald, B.E., et al., *Recent Progress in High Entropy Alloy Research*. *JOM*, 2017. **69**(10): p. 2024-2031.
23. Porter, D.A., K.E. Easterling, and M. Sherif, *Phase Transformations in Metals and Alloys, (Revised Reprint)*. 2009: CRC press.
24. Miracle, D. and O. Senkov, *A critical review of high entropy alloys and related concepts*. *Acta Materialia*, 2017. **122**: p. 448-511.
25. Lucas, M.S., et al., *Absence of long-range chemical ordering in equimolar FeCoCrNi*. *Applied Physics Letters*, 2012. **100**(25): p. 251907.
26. Swalin, R.A., *Thermodynamics of Solids, 2nd Ed.* 1991, New York: Wiley.
27. Gaskell, D.R., *Introduction to the Thermodynamics of Materials*. 2008: CRC Press.
28. Miracle, D.B., et al., *Exploration and development of high entropy alloys for structural applications*. *Entropy*, 2014. **16**(1): p. 494-525.
29. Yeh, J.W., *Alloy Design Strategies and Future Trends in High-Entropy Alloys*. *Jom*, 2013. **65**(12): p. 1759-1771.
30. Gao, M.C., et al., *High-Entropy Alloys: Fundamentals and Applications*. 2016, Cham, Switzerland: Springer.
31. Tsai, K.Y., M.H. Tsai, and J.W. Yeh, *Sluggish diffusion in Co-Cr-Fe-Mn-Ni high-entropy alloys*. *Acta Materialia*, 2013. **61**(13): p. 4887-4897.
32. Tong, C.J., et al., *Microstructure characterization of Al<sub>x</sub>CoCrCuFeNi high-entropy alloy system with multiprincipal elements*. *Metallurgical and Materials Transactions A*, 2005. **36**(4): p. 881-893.
33. Dirras, G., et al., *Elastic and plastic properties of as-cast equimolar TiHfZrTaNb high-entropy alloy*. *Materials Science and Engineering A*, 2016. **654**: p. 30-38.
34. Yeh, J.W., et al., *Anomalous decrease in X-ray diffraction intensities of Cu-Ni-Al-Co-Cr-Fe-Si alloy systems with multi-principal elements*. *Materials Chemistry and Physics*, 2007. **103**(1): p. 41-46.
35. Yeh, J.W., et al., *Formation of simple crystal structures in Cu-Co-Ni-Cr-Al-Fe-Ti-V alloys with multiprincipal metallic elements*. *Metallurgical and Materials Transactions A*, 2004. **35**(8): p. 2533-2536.
36. Zhang, Y., et al., *Minor alloying behavior in bulk metallic glasses and high-entropy alloys*. *Science in China Series G-Physics Mechanics & Astronomy*, 2008. **51**(4): p. 427-437.
37. Guo, S., et al., *Effect of valence electron concentration on stability of fcc or bcc phase in high entropy alloys*. *Journal of Applied Physics*, 2011. **109**(10): p. 103505.
38. Zhang, Y., et al., *Solid-solution phase formation rules for multi-component alloys*. *Advanced Engineering Materials*, 2008. **10**(6): p. 534-538.
39. Zhang, Y., X. Yang, and P.K. Liaw, *Alloy design and properties optimization of high-entropy alloys*. *JOM*, 2012. **64**(7): p. 830-838.
40. Yang, X. and Y. Zhang, *Prediction of high-entropy stabilized solid-solution in multi-component alloys*. *Materials Chemistry and Physics*, 2012. **132**(2-3): p. 233-238.
41. Guo, S., et al., *More than entropy in high-entropy alloys: Forming solid solutions or amorphous phase*. *Intermetallics*, 2013. **41**: p. 96-103.
42. Davis, J.R., *ASM Specialty Handbook: Nickel, Cobalt, and Their Alloys*. 2000, Materials Park, OH: ASM International.

43. Morinaga, M., et al., *Solid solubilities in transition-metal-based fcc alloys*. Philosophical Magazine A, 1985. **51**(2): p. 223-246.
44. Adachi, H., T. Mukoyama, and J. Kawai, *Hartree–Fock–Slater Method for Materials Science: The DV-X $\alpha$  Method for Design and Characterization of Materials*. 2005, Berlin: Springer. 23-48.
45. Bozzolo, G., R.D. Noebe, and P.B. Abel, *Applied Computational Materials Modeling: Theory, Simulation and Experiment*. 2007: Springer Science & Business Media.
46. Morinaga, M., et al., *New PHACOMP and its application to alloy design*. Superalloys 1984, 1984: p. 523-532.
47. Hsu, Y.J., W.C. Chiang, and J.W. Wu, *Corrosion behavior of FeCoNiCrCu<sub>x</sub> high-entropy alloys in 3.5% sodium chloride solution*. Materials Chemistry and Physics, 2005. **92**(1): p. 112-117.
48. Zhang, Y., G.L. Chen, and L. Gan, *Phase change and mechanical behaviors of Ti<sub>x</sub>CoCrFeNiCu<sub>1-y</sub>Al<sub>y</sub> high entropy alloys*. Journal of ASTM International, 2010. **7**(5): p. Paper ID: JAI102527
49. Liu, W.H., et al., *Ductile CoCrFeNiMox high entropy alloys strengthened by hard intermetallic phases*. Acta Materialia, 2016. **116**: p. 332-342.
50. Shun, T.T., L.Y. Chang, and M.H. Shiu, *Microstructure and mechanical properties of multiprincipal component CoCrFeNiMo<sub>x</sub> alloys*. Materials Characterization, 2012. **70**: p. 63-67.
51. Shun, T.T., L.Y. Chang, and M.H. Shiu, *Microstructures and mechanical properties of multiprincipal component CoCrFeNiTi<sub>x</sub> alloys*. Materials Science and Engineering A, 2012. **556**: p. 170-174.
52. Wang, X.F., et al., *Novel microstructure and properties of multicomponent CoCrCuFeNiTi<sub>x</sub> alloys*. Intermetallics, 2007. **15**(3): p. 357-362.
53. Chuang, M.H., et al., *Microstructure and wear behavior of Al<sub>x</sub>Co<sub>1.5</sub>CrFeNi<sub>1.5</sub>Ti<sub>y</sub> high-entropy alloys*. Acta Materialia, 2011. **59**(16): p. 6308-6317.
54. Shun, T.T., C.H. Hung, and C.F. Lee, *The effects of secondary elemental Mo or Ti addition in Al<sub>0.3</sub>CoCrFeNi high-entropy alloy on age hardening at 700 °C*. Journal of Alloys and Compounds, 2010. **495**(1): p. 55-58.
55. Lukas, H.L., S.G. Fries, and B. Sundman, *Computational Thermodynamics - The Calphad Method*. Cambridge University Press.
56. Saunders, N., A.P. Miodownik, and A.P. Miodownik, *CALPHAD (Calculation of Phase Diagrams): A Comprehensive Guide*. 1998, London, UNITED KINGDOM: Elsevier Science.
57. Ming, K., X. Bi, and J. Wang, *Precipitation strengthening of ductile Cr15Fe20Co35Ni20Mo10 alloys*. Scripta Materialia, 2017. **137**: p. 88-93.
58. Chen, H.Y., et al., *Effect of the substitution of Co by Mn in Al-Cr-Cu-Fe-Co-Ni high-entropy alloys*. Annales De Chimie-Science Des Materiaux, 2006. **31**(6): p. 685-698.
59. Chen, M.R., et al., *Microstructure and properties of Al<sub>0.5</sub>CoCrCuFeNiTi<sub>x</sub> (x=0-2.0) high-entropy alloys*. Materials Transactions, 2006. **47**(5): p. 1395-1401.
60. Ma, S.G. and Y. Zhang, *Effect of Nb addition on the microstructure and properties of AlCoCrFeNi high-entropy alloy*. Materials Science and Engineering A, 2012. **532**: p. 480-486.
61. Shun, T.T. and Y.C. Du, *Microstructure and tensile behaviors of FCC Al<sub>0.3</sub>CoCrFeNi high entropy alloy*. Journal of Alloys and Compounds, 2009. **479**(1-2): p. 157-160.

62. Daoud, H.M., et al., *Microstructure and Tensile Behavior of Al<sub>8</sub>Co<sub>17</sub>Cr<sub>17</sub>Cu<sub>8</sub>Fe<sub>17</sub>Ni<sub>33</sub> (at.%) High-Entropy Alloy*. Jom, 2013. **65**(12): p. 1805-1814.
63. Wang, F.J., et al., *Tensile and compressive mechanical behavior of a CoCrCuFeNiAl<sub>0.5</sub> high entropy alloy*. International Journal of Modern Physics B, 2009. **23**(6-7): p. 1254-1259.
64. Kuznetsov, A.V., et al., *Tensile properties of an AlCrCuNiFeCo high-entropy alloy in as-cast and wrought conditions*. Materials Science and Engineering A, 2012. **533**: p. 107-118.
65. Gludovatz, B., et al., *A fracture-resistant high-entropy alloy for cryogenic applications*. Science, 2014. **345**(6201): p. 1153-1158.
66. Hemphill, M.A., et al., *Fatigue behavior of Al<sub>0.5</sub>CoCrCuFeNi high entropy alloys*. Acta Materialia, 2012. **60**(16): p. 5723-5734.
67. Burkhanov, E.M.S.S., *Physical Metallurgy of Refractory Metals and Alloys*. 1995: Springer, Boston, MA.
68. [www.vertex42.com/Files/pdfs/2/periodic-table.pdf](http://www.vertex42.com/Files/pdfs/2/periodic-table.pdf).
69. Yang, X., Y. Zhang, and P.K. Liaw, *Microstructure and Compressive Properties of NbTiVTaAl<sub>x</sub> High Entropy Alloys*. Iumrs International Conference in Asia 2011, 2012. **36**: p. 292-298.
70. Fazakas, E., et al., *Experimental and theoretical study of Ti<sub>20</sub>Zr<sub>20</sub>Hf<sub>20</sub>Nb<sub>20</sub>X<sub>20</sub> (X = V or Cr) refractory high-entropy alloys*. International Journal of Refractory Metals & Hard Materials, 2014. **47**: p. 131-138.
71. [www.haynesintl.com/230HaynesAlloy.htm](http://www.haynesintl.com/230HaynesAlloy.htm).
72. [www.specialmetals.com/inconel-alloy-718](http://www.specialmetals.com/inconel-alloy-718).
73. Wu, Y.D., et al., *A refractory Hf<sub>25</sub>Nb<sub>25</sub>Ti<sub>25</sub>Zr<sub>25</sub> high-entropy alloy with excellent structural stability and tensile properties*. Materials Letters, 2014. **130**: p. 277-280.
74. Huang, H., et al., *Phase-Transformation Ductilization of Brittle High-Entropy Alloys via Metastability Engineering*. Advanced Materials, 2017. **29**(30): p. 1701678-n/a.
75. Liu, G., et al., *Nanostructured high-strength molybdenum alloys with unprecedented tensile ductility*. Nature materials, 2013. **12**(4): p. 344-350.
76. Rice, J.R. and R. Thomson, *Ductile versus brittle behaviour of crystals*. Philosophical magazine, 1974. **29**(1): p. 73-97.
77. Chan, K.S., *A computational approach to designing ductile Nb-Ti-Cr-Al solid-solution alloys*. Metallurgical and Materials Transactions A, 2001. **32**(10): p. 2475-2487.
78. Peierls, R., *The size of a dislocation*. Proceedings of the Physical Society, 1940. **52**(1): p. 34.
79. Nabarro, F., *Dislocations in a simple cubic lattice*. Proceedings of the Physical Society, 1947. **59**(2): p. 256.
80. Qi, L. and D.C. Chrzan, *Tuning ideal tensile strengths and intrinsic ductility of bcc refractory alloys*. Physical Review Letters, 2014. **112**(11): p. 115503.
81. Liu, C.T. and J.O. Stiegler, *Ductile ordered intermetallic alloys*. Science, 1984. **226**(4675): p. 636-642.
82. Mizutani, U., *Hume-Rothery Rules for Structurally Complex Alloy Phases*. 2011, Boca Raton: CRC Press.
83. Massalski, T.B., *Comments concerning some features of phase diagrams and phase transformations*. Materials Transactions, 2010. **51**(4): p. 583-596.

84. Senkov, O.N. and S.L. Semiatin, *Microstructure and properties of a refractory high-entropy alloy after cold working*. Journal of Alloys and Compounds, 2015. **649**: p. 1110-1123.
85. Dieter, G.E., *Mechanical Metallurgy*. Vol. 3. 1976, New York: McGraw-Hill
86. Kofstad, P., *High Temperature Oxidation of Metals*. 1966: John Wiley & Son, New York.
87. Kim, B.G., G.M. Kim, and C.J. Kim, *Oxidation behavior of TiAl-X (X = Cr, V, Si, Mo or Nb) intermetallics at elevated temperature*. Scripta Metallurgica et Materialia, 1995. **33**(7): p. 1117-1125.
88. Zelenitsas, K. and P. Tsakiroopoulos, *Effect of Al, Cr and Ta additions on the oxidation behaviour of Nb-Ti-Si in situ composites at 800°C*. Materials Science and Engineering: A, 2006. **416**(1): p. 269-280.
89. Chan, K.S., *Alloying effects on fracture mechanisms in Nb-based intermetallic in-situ composites*. Materials Science and Engineering a-Structural Materials Properties Microstructure and Processing, 2002. **329**: p. 513-522.
90. Lemberg, J.A. and R.O. Ritchie, *Mo-Si-B alloys for ultrahigh-temperature structural applications*. Advanced Materials, 2012. **24**(26): p. 3445-3480.
91. Liu, C.M., et al., *Microstructure and oxidation behavior of new refractory high entropy alloys*. Journal of Alloys and Compounds, 2014. **583**: p. 162-169.
92. Senkov, O.N., et al., *Oxidation behavior of a refractory NbCrMo<sub>0.5</sub>Ta<sub>0.5</sub>TiZr alloy*. Journal of Materials Science, 2012. **47**(18): p. 6522-6534.
93. Gorr, B., et al., *High-Temperature Oxidation Behavior of Refractory High-Entropy Alloys: Effect of Alloy Composition*. Oxidation of Metals, 2017. **88**(3): p. 339-349.
94. Chen, H., et al., *Microstructure and mechanical properties at elevated temperatures of a new Al-containing refractory high-entropy alloy Nb-Mo-Cr-Ti-Al*. Journal of Alloys and Compounds, 2016. **661**: p. 206-215.
95. B. Gorr, F.M., H.-J. Christ, T. Mueller, H. Chen, A. Kauffmann, M. Heilmaier, *High temperature oxidation behavior of an equimolar refractory metal-based alloy Nb<sub>20</sub>Mo<sub>20</sub>Cr<sub>20</sub>Ti<sub>20</sub>Al<sub>20</sub> with and without Si addition*. Journal of Alloys and Compounds, 2016. **688**: p. 468-477.
96. Zhang, Z.T., et al., *Microstructure, mechanical properties and corrosion resistance of CuZrY/Al, Ti, Hf series high-entropy alloys*. Materials & Design, 2016. **108**: p. 106-113.
97. Westbrook, J.H. and D.L. Wood, *"PEST" degradation in beryllides, silicides, aluminides, and related compounds*. Journal of Nuclear Materials, 1964. **12**(2): p. 208-215.
98. Tolpygo, V.K. and H.J. Grabke, *Mechanism of the intergranular disintegration (pest) of the intermetallic compound NbAl<sub>3</sub>*. Scripta Metallurgica et Materialia, 1993. **28**(6): p. 747-752.
99. McKamey, C.G., et al., *A study of pest oxidation in polycrystalline MoSi<sub>2</sub>*. Journal of Materials Research, 2011. **7**(10): p. 2747-2755.
100. Grabke, H.J.a.G.H.M., *Accelerated oxidation, internal oxidation, intergranular oxidation, and pesting of intermetallic compounds*. Oxidation of Metals, 1995: p. 147 - 176.
101. Chou, T.C. and T.G. Nieh, *Mechanism of MoSi<sub>2</sub> pest during low temperature oxidation*. Journal of Materials Research, 2016. **8**(1): p. 214-226.
102. Stern, K.H.E., *Metallurgical and Ceramic Protective Coatings*. 1996, Springer Netherlands.
103. Wöllmer, S., et al., *Characterization of phases of aluminized nickel base superalloys*. Surface and Coatings Technology, 2003. **167**(1): p. 83-96.

104. Li, H., M. Qiao, and C. Zhou, *Formation and cyclic oxidation resistance of Hf-Co-modified aluminide coatings on nickel base superalloys*. Materials Chemistry and Physics, 2014. **143**(3): p. 915-920.
105. Kasai, K., et al., *Effect of Surface Treatment and Crystal Orientation on Microstructural Changes in Aluminized Ni-Based Single-Crystal Superalloy*. MATERIALS TRANSACTIONS, 2011. **52**(9): p. 1768-1772.
106. Cockeram, B.V., *Growth and oxidation resistance of boron-modified and germanium-doped silicide diffusion coatings formed by the halide-activated pack cementation method*. Surface and Coatings Technology, 1995. **76-77**: p. 20-27.
107. Koo, C.H. and T.H. Yu, *Pack cementation coatings on Ti3Al-Nb alloys to modify the high-temperature oxidation properties*. Surface and Coatings Technology, 2000. **126**(2): p. 171-180.
108. Li, Y., W. Soboyejo, and R.A. Rapp, *Oxidation behavior of niobium aluminide intermetallics protected by aluminide and silicide diffusion coatings*. Metallurgical and Materials Transactions B, 1999. **30**(3): p. 495-504.
109. Goward, G.W. and D.H. Boone, *Mechanisms of formation of diffusion aluminide coatings on nickel-base superalloys*. Oxidation of Metals, 1971. **3**(5): p. 475-495.
110. Hocking MG, V.V., Sidky PS., *Metallic and ceramic coatings: production, high temperature properties and applications*. 1989: Longman: Essex (UK) and John Wiley & Sons: New York.
111. Kung, S.C., *High-temperature coating for titanium aluminides using the pack-cementation technique*. Oxidation of Metals, 1990. **34**(3): p. 217-228.
112. Zhou, C., et al., *A study of aluminide coatings on TiAl alloys by the pack cementation method*. Materials Science and Engineering: A, 2003. **341**(1): p. 169-173.
113. Tsai, C.-W., et al., *Isothermal Oxidation of Aluminized Coatings on High-Entropy Alloys*. Entropy, 2016. **18**(10): p. 376.
114. Kelly, A., G.W. Groves, and P. Kidd, *Crystallography and Crystal Defects*. 2000: John Wiley & Sons.
115. Goldstein, J., *Practical Scanning Electron Microscopy: Electron and Ion Microprobe Analysis*. 2012: Springer Science & Business Media.
116. V. Sass, U.G., M. Feller-Kniepmeier, in: R.D. Kissinger, et al. (Eds.), *Creep anisotropy in the monocrystalline nickel-base superalloy* Superalloys, TMS, Warrendale, PA, 1996: p. 283.
117. Britton, T.B., et al., *Tutorial: Crystal orientations and EBSD — Or which way is up?* Materials Characterization, 2016. **117**: p. 113-126.
118. Grimwade, M., *THE METALLURGY OF GOLD*. Interdisciplinary Science Reviews, 1992. **17**(4): p. 371-381.
119. Liu, W.H., et al., *Effects of Nb additions on the microstructure and mechanical property of CoCrFeNi high-entropy alloys*. Intermetallics, 2015. **60**: p. 1-8.
120. Massalski, T.B., et al., *Binary Alloy Phase Diagrams. vol. 3*. ASM International, 1990, 1990.
121. Yeh, J.W., et al., *High-entropy alloys - A new era of exploitation*. Materials Science Forum, 2007. **560**: p. 1-9.
122. Juan, C.C., et al., *Enhanced mechanical properties of HfMoTaTiZr and HfMoNbTaTiZr refractory high-entropy alloys*. Intermetallics, 2015. **62**: p. 76-83.
123. Guo, N.N., et al., *Microstructure and mechanical properties of refractory MoNbHfZrTi high-entropy alloy*. Materials & Design, 2015. **81**: p. 87-94.

124. Yao, H.W., et al., *MoNbTaV medium-entropy alloy*. Entropy, 2016. **18**(5): p. doi:10.3390/e18050189.
125. Ashby, M.F., *Materials Selection in Mechanical Design, Fourth Edition*. 2011, Amsterdam: Elsevier.
126. Otto, F., N.L. Hanold, and E.P. George, *Microstructural evolution after thermomechanical processing in an equiatomic, single-phase CoCrFeMnNi high-entropy alloy with special focus on twin boundaries*. Intermetallics, 2014. **54**: p. 39-48.
127. Senkov, O.N. and D.B. Miracle, *Effect of the atomic size distribution on glass forming ability of amorphous metallic alloys*. Materials Research Bulletin, 2001. **36**(12): p. 2183-2198.
128. Sheikh, S., et al., *Alloy design for intrinsically ductile refractory high-entropy alloys*. Journal of Applied Physics, 2016. **120**(16): p. 164902.
129. Nieh, T.G. and W.D. Nix, *Embrittlement of copper due to segregation of oxygen to grain boundaries*. Metallurgical Transactions A, 1981. **12**(5): p. 893-901.

